Atmospheric
Chemistry
and Physics

Open Access

EGU

Validation of OMI, GOME-2A and GOME-2B tropospheric NO$_2$, SO$_2$ and HCHO products using MAX-DOAS observations from 2011 to 2014 in Wuxi, China: investigation of the effects of priori profiles and aerosols on the satellite products

Yang Wang[1], Steffen Beirle[1], Johannes Lampel[1,2], Mariliza Koukouli[3], Isabelle De Smedt[4], Nicolas Theys[4], Ang Li[5], Dexia Wu[5], Pinhua Xie[5,6,7], Cheng Liu[8,6,5], Michel Van Roozendael[4], Trissevgeni Stavrakou[4], Jean-François Müller[4], and Thomas Wagner[1]

[1]Max Planck Institute for Chemistry, Mainz, Germany
[2]Institute of Environmental Physics, University of Heidelberg, Heidelberg, Germany
[3]Laboratory of Atmospheric Physics, Aristotle University of Thessaloniki, Thessaloniki, Greece
[4]Belgian Institute for Space Aeronomy (BIRA-IASB), Brussels, Belgium
[5]Anhui Institute of Optics and Fine Mechanics, Chinese Academy of Sciences, Hefei, China
[6]CAS Center for Excellence in Urban Atmospheric Environment, Institute of Urban Environment, Chinese Academy of Sciences, Xiamen, China
[7]School of Environmental Science and Optoelectronic Technology, University of Science and Technology of China, Hefei, China
[8]School of Earth and Space Sciences, University of Science and Technology of China, Hefei, China

Correspondence to: Yang Wang (y.wang@mpic.de), Ang Li (angli@aiofm.ac.cn)
and Cheng Liu (chliu81@ustc.edu.cn)

Abstract. Tropospheric vertical column densities (VCDs) of NO$_2$, SO$_2$ and HCHO derived from the Ozone Monitoring Instrument (OMI) on AURA and the Global Ozone Monitoring Experiment 2 aboard METOP-A (GOME-2A) and METOP-B (GOME-2B) are widely used to characterize the global distributions, trends and dominating sources of these trace gases. They are also useful for the comparison with chemical transport models (CTMs). We use tropospheric VCDs and vertical profiles of NO$_2$, SO$_2$ and HCHO derived from MAX-DOAS measurements from 2011 to 2014 in Wuxi, China, to validate the corresponding products (daily and bi-monthly-averaged data) derived from OMI and GOME-2A/B by different scientific teams. Prior to the comparison, the spatial and temporal coincidence criteria for MAX-DOAS and satellite data are determined by a sensitivity study using different spatial and temporal averaging conditions. Cloud effects on both MAX-DOAS and satel-

lite observations are also investigated. Our results indicate that the discrepancies between satellite and MAX-DOAS results increase with increasing effective cloud fraction and are dominated by the effects of clouds on the satellite products. In comparison with MAX-DOAS, we found a systematic underestimation of all SO$_2$ (40 to 57 %) and HCHO products (about 20 %), and an overestimation of the GOME-2A/B NO$_2$ products (about 30 %), but good consistency with the DOMINO version 2 NO$_2$ product. To better understand the reasons for these differences, we evaluated the a priori profile shapes used in the OMI retrievals (derived from CTM) by comparison with those derived from the MAX-DOAS observations. Significant differences are found for the SO$_2$ and HCHO profile shapes derived from the IMAGES model, whereas on average good agreement is found for the NO$_2$ profile shapes derived from the TM4 model. We also applied the MAX-DOAS profile shapes to the satellite re-

trievals and found that these modified satellite VCDs agree better with the MAX-DOAS VCDs than the VCDs from the original data sets by up to 10, 47 and 35 % for NO$_2$, SO$_2$ and HCHO, respectively. Furthermore, we investigated the effect of aerosols on the satellite retrievals. For OMI observations of NO$_2$, a systematic underestimation is found for large AOD, which is mainly attributed to effect of the aerosols on the cloud retrieval and the subsequent application of a cloud correction scheme (implicit aerosol correction). In contrast, the effect of aerosols on the clear-sky air mass factor (explicit aerosol correction) has a smaller effect. For SO$_2$ and HCHO observations selected in the same way, no clear aerosol effect is found, probably because for the considered data sets no cloud correction is applied (and also because of the larger scatter). From our findings we conclude that for satellite observations with cloud top pressure (CTP) > 900 hPa and effective cloud fraction (eCF) < 10 % the application of a clear-sky air mass factor might be a good option if accurate aerosol information is not available. Another finding of our study is that the ratio of morning-to-afternoon NO$_2$ VCDs can be considerably overestimated if results from different sensors and/or retrievals (e.g. OMI and GOME-2) are used, whereas fewer deviations for HCHO and SO$_2$ VCDs are found.

1 Introduction

Nitrogen oxides (NO$_x$ ≡ NO$_2$ + NO), sulphur dioxide (SO$_2$) and formaldehyde (HCHO) play critical roles in tropospheric chemistry through various gas phase and multi-phase chemical reactions (Seinfeld and Pandis, 1998). In an urban and industrialized region, anthropogenic emissions from traffic, domestic heating, factories, power plants and biomass burning significantly elevate the concentrations of these (and other) trace gases (TGs) in the boundary layer (Environmental Protection Agency, 1998; Seinfeld and Pandis, 1998). There is strong evidence that aerosol particles formed through photochemistry of NO$_x$, SO$_2$ and VOCs significantly contribute to haze pollution events occurring frequently around megacities and urban agglomerations in China, like the Jing–Jin–Ji region and the Yangtze River delta region (Crippa et al., 2014; Huang et al., 2014; Jiang et al., 2015; Fu et al., 2014). The aerosols also impact the local radiative forcing through direct (e.g. McCormic and Ludwig, 1967) and indirect effects (Lohmann and Feichter, 2005). Understanding global and regional distributions and temporal variations of the TGs, and further identifying and quantifying their dominant sources, can provide a firm basis for a better understanding of the formation mechanisms of haze pollution and for the development of mitigation strategies.

Since 1995 a series of sun-synchronous satellites, such as ERS-2, ENVISAT, AURA, METOP-A and METOP-B, was launched carrying UV, visible or NIR spectrometers with moderate spectral resolution, which allowed scientists to determine global distributions of several important tropospheric TGs including NO$_2$, HCHO and SO$_2$ for the first time. The first instrument was the Global Ozone Monitoring Experiment (GOME) (Burrows et al., 1999), followed by the Scanning Imaging Absorption Spectrometer for Atmospheric Chartography (SCIAMACHY) (e.g. Bovensmann et al., 1999), the Ozone Monitoring Instrument (OMI) (Levelt et al., 2006a, b), and the GOME-2A and GOME-2B instruments (Callies et al., 2000; Munro et al., 2006, 2016). The OMI and GOME-2A/B instruments are still in operation. A large number of studies developed retrieval algorithms for these instruments to acquire the tropospheric vertical column densities (VCDs) of NO$_2$ (e.g. Boersma et al., 2004, 2007, 2011; Richter et al., 2005; Beirle and Wagner, 2012; Valks et al., 2011), SO$_2$ (e.g. Krueger et al., 1995; Eisinger and Burrows, 1998; Carn et al., 2004; Krotkov et al., 2006; Richter et al., 2006, 2009; Yang et al., 2007; Lee et al., 2009; Nowlan et al., 2011; Rix et al., 2012; C. Li et al., 2013; Theys et al., 2015) and HCHO (Chance et al., 2000; Palmer et al., 2001; Wittrock et al., 2006a; De Smedt et al., 2008, 2012, 2015; Kurosu, 2008; Millet et al., 2008; Hewson et al., 2013; González Abad et al., 2015). In this validation study we include several products, which have been published recently and are widely used: for NO$_2$ the near-real-time OMI DOMINO v2.0 (Boersma et al., 2007, 2011) and the GOME-2A/B TM4NO2A (Boersma et al., 2004); for SO$_2$ the operational OMSO2 OMI product (C. Li et al., 2013) published by National Aeronautics and Space Administration (NASA), the O3M-SAF operational GOME-2A product published by the German Aerospace Centre (DLR) (Rix et al., 2012; Hassinen et al., 2016), and the OMI and GOME-2A/B products developed by BIRA (Theys et al., 2015); and for HCHO the OMI and GOME-2A/B products developed by BIRA (De Smedt et al., 2008, 2012, 2015). Many users already benefit from these products for several applications, e.g. detection and quantification of emissions, identification of transport processes and chemical transformations, and for the comparison with model simulations (e.g. Beirle et al., 2003, 2011; Martin et al., 2003; Richter et al., 2005; van der A et al., 2008; Herron-Thorpe et al., 2010; Gonzi et al., 2011; Barkley et al., 2012; Koukouli et al., 2016).

Although several studies have made efforts to improve satellite retrievals, significant differences compared to ground-based measurements were still reported by several validation studies, e.g. a systematic underestimation of the tropospheric VCDs of NO$_2$, SO$_2$ and HCHO was obtained for OMI by > 30 % in or near Beijing, China (Ma et al., 2013; Theys et al., 2015; De Smedt et al., 2015; Jin et al., 2016). The satellite retrieval errors are mainly attributed to the slant column retrievals (spectral analysis), the stratospheric correction (for NO$_2$) and the tropospheric air mass factor (AMF) calculations. The AMF uncertainties are related to several factors, such as the surface albedo, the cloud and aerosol properties, methodological assumptions on how clouds and aerosols should be accounted for (Lin et al., 2015), the a pri-

ori profile shape (also referred to as the shape factor (SF) in the following), and interpolation errors of the discrete look-up table entries (Lin et al., 2014). Thus validation studies for satellite products using independent ground-based measurements are essential to quantify uncertainties, identify dominant error sources and to further improve the satellite retrieval algorithms.

Since about 15 years ago, the Multi-Axis Differential Optical Absorption Spectroscopy (MAX-DOAS) technique (Hönninger and Platt, 2002; Bobrowski et al., 2003; Van Roozendael et al., 2003; Hönninger et al., 2004; Wagner et al., 2004; Wittrock et al., 2004) is applied to retrieve tropospheric vertical profiles of TGs and aerosols from spectra of scattered UV and visible sunlight measured at different elevation angles (e.g. Frieß et al., 2006, 2011, 2016; Wittrock et al., 2006b; Irie et al., 2008, 2011; Clémer et al., 2010; Li et al., 2010, X. Li et al., 2013; Vlemmix et al., 2010, 2011, 2015b; Wagner et al., 2011; Yilmaz, 2012; Hartl and Wenig, 2013; Wang et al., 2013a, b). MAX-DOAS observations provide valuable information that can be applied for a quantification of air pollutants (e.g. X. Li et al., 2013; Hendrick et al., 2014; Wang et al., 2014, 2017), a validation of tropospheric satellite products (e.g. Irie et al., 2012, 2016; Ma et al., 2013; Kanaya et al., 2014; Theys, et al., 2015; De Smedt et al., 2015; Jin et al., 2016) and an evaluation of chemical transport model (CTM) simulations (e.g. Vlemmix et al., 2015a). The tropospheric vertical profiles are also valuable for the evaluation of SFs used in the satellite AMF calculations. Here it is important to note that many studies already investigated the effect of the a priori SFs on the satellite retrievals (i.e. Boersma et al., 2004; Hains et al., 2010; Heckel et al., 2011) and demonstrated that the SF effect on the tropospheric AMFs can dominate the systematic errors of tropospheric satellite products, especially in highly polluted (urban and industrial) regions (Boersma et al., 2011; Theys et al., 2015; De Smedt et al., 2015). Nevertheless, because profile measurements are rare, the SF effect is still not well understood in many regions. In this study the SF effect on the tropospheric AMF will be investigated using the vertical profiles of the TGs derived from the MAX-DOAS observations in Wuxi, China, from 2011 to 2014 (Wang et al., 2017).

Wuxi is located about 130 km north-west of Shanghai and belongs to the most industrialized part of the Yangtze River delta (YRD) region. The YRD, including Shanghai City and four nearby provinces, is the largest economic region in China. It is heavily industrialized and can be considered as the largest metropolitan area in Asia, with a population of about 150 million. Several studies already used satellite products of the pollutants to quantify the corresponding emissions (Ding et al., 2015; Han et al., 2015; Bauwens et al., 2016) in this region. However, validation studies for the satellite products in this region are still sparse. Chen et al. (2009), Irie et al. (2012), Kanaya et al. (2014) and Chan et al. (2015) validated the satellite NO₂ tropospheric VCD products using MAX-DOAS (or zenith-sky DOAS) measurements in Rudong, Hefei and Shanghai. So far there are no validation reports for SO₂ and HCHO products in the YRD region. However, several validation studies have been carried out in other regions of China (e.g. Theys et al., 2015; De Smedt et al., 2015; Jin et al., 2016).

In this study we validate daily (2 h around the satellite overpass time) and bi-monthly averages of the tropospheric VCDs of NO₂, SO₂ and HCHO derived from OMI and GOME-2 using the MAX-DOAS observations in Wuxi, and we discuss in particular the influence of the coincidence criteria on the comparison results. Previous studies (Ma et al., 2013; Jin et al., 2016) already presented comparison studies and discussed several aspects limiting the consistency between satellite and MAX-DOAS observations. Concerning the impact of clouds on both MAX-DOAS and satellite retrievals, we separately evaluate the cloud effects on both satellite and MAX-DOAS observations. Also, the weekend effect and ratios of morning and afternoon values (representing diurnal variations) acquired by combining GOME-2 and OMI observations are evaluated by comparison with similar ratios derived from the corresponding MAX-DOAS results.

For most of the satellite products, aerosol information is not considered in radiative transfer models (RTMs) used for the AMF calculations (one exception is the OMI NO₂ product (POMINO) provided by the Peking University over China; Lin et al., 2014), but recently such aerosol effects have drawn more and more attention. Shaiganfar et al. (2011), Ma et al. (2013), and Kanaya et al. (2014) found negative biases of the OMI tropospheric NO₂ VCDs between 26 and 50 % over areas with high aerosol pollution through the validation by MAX-DOAS observations. But aerosol effects on the satellite retrievals are still not well understood. The aerosol effects can be generally separated into two contributions: (a) the effect of aerosols on the satellite AMF compared to AMFs for a pure Rayleigh atmosphere (explicit aerosol correction), and (b) the effect of aerosols on the retrieval of cloud products (often referred to as "implicit aerosol correction", Boersma et al., 2011; Castellanos et al., 2015; Chimot et al., 2016). These two contributions of aerosols on the satellite retrievals are discussed in this study based on the aerosol and TG profiles derived from the MAX-DOAS observations in Wuxi and by comparing the satellite TG VCDs to the corresponding results from the MAX-DOAS observations.

The paper is organized as follows: in Sect. 2 we describe the MAX-DOAS observations in Wuxi and the satellite products involved in this study. In Sect. 3 we compare the NO₂, SO₂ and HCHO VCDs derived from MAX-DOAS with those from the satellite instruments. We investigate in particular the effects of clouds, SFs and aerosols on the satellite retrievals. In Sect. 4 the conclusions are given.
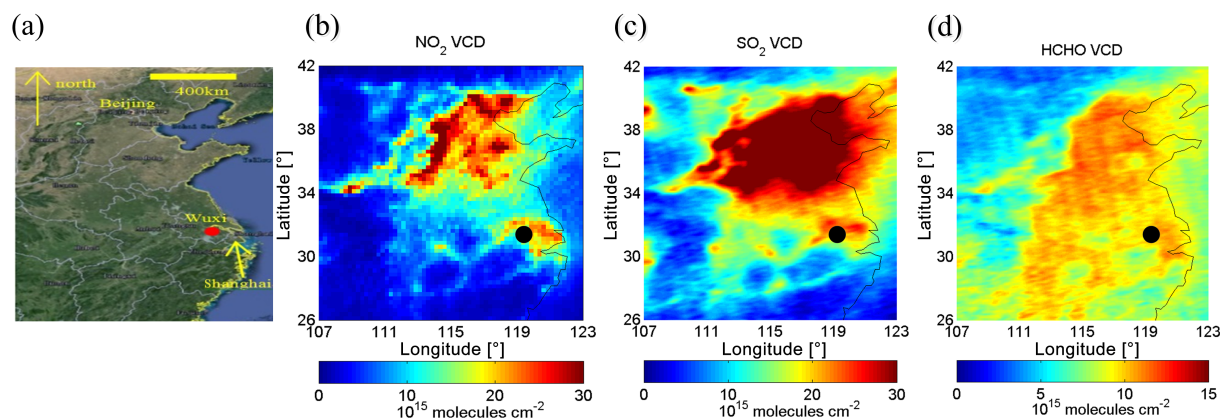
Figure 1. Wuxi city, in which the MAX-DOAS instrument is operated, is marked by the red dot in **(a)**. Panels **(b)**, **(c)** and **(d)** show maps of the averaged tropospheric VCDs of NO$_2$ from DOMINO 2, SO$_2$ and HCHO from BIRA, derived from OMI observations over eastern China in the period from 2011 to 2014, respectively. The black dots indicate the location of Wuxi.

2   MAX-DOAS measurements and satellite data sets

2.1   MAX-DOAS instrument and data analysis

A MAX-DOAS instrument developed by the Anhui Institute of Optics and Fine Mechanics (AIOFM) (Wang et al., 2015, 2017) is located on the roof of an 11-storey building in Wuxi City (Fig. 1a), China (31.57° N, 120.31° E, 50 m a.s.l.), and operated by the Wuxi CAS Photonics Co. Ltd from May 2011 to December 2014. Wuxi City is located in the YRD region which is typically affected by high loads of NO$_2$, SO$_2$ and HCHO (Fig. 1b, c, d). The DOAS method (Platt and Stutz, 2008) and the PriAM profile inversion algorithm (Wang et al., 2013a, b, 2017) are applied to derive the vertical profiles of aerosol extinction (AE) and volume mixing ratios (VMRs) of NO$_2$, SO$_2$ and HCHO from scattered UV and visible sunlight recorded by the MAX-DOAS instrument at five elevation angles (5, 10, 20, 30 and 90°). The telescope of the instrument is pointed to the north. The data analysis and the results derived from the MAX-DOAS measurements are already described in our previous study (Wang et al., 2017). In that study we compared the MAX-DOAS results with collocated independent techniques including an AERONET sun photometer, a visibility meter, and a long path DOAS. The comparisons were done for different cloud conditions as derived from a cloud classification scheme based on the MAX-DOAS observations (Wagner et al., 2014; Wang et al., 2015). One important conclusion of that study was that meaningful TG profiles can be retrieved not only for clear skies, but also for most cloudy conditions (except for heavy fog or haze and optically thick clouds). Thus in this study we use all MAX-DOAS TG profiles obtained for these sky conditions (Wang et al., 2017). Here it is important to note that, differently from previous studies (e.g. Ma et al., 2013; Jin et al., 2016), we derive the tropospheric VCDs of the TGs by an integration of the vertical

profiles, but not by the so-called geometric approximation (e.g. Brinksma et al., 2008). Our previous study (Wang et al., 2017) demonstrated that the tropospheric TG VCDs from the full profile inversion are in general more accurate than those from the geometric approximation. The discrepancy of the VCDs derived by both methods is systematic and can be mainly attributed to the errors of the geometric approximation, for which the errors can be up to 30 % depending on the observation geometry, and the properties of aerosols and TGs.

2.2   NO$_2$, SO$_2$ and HCHO products derived from OMI

The OMI instrument (Levelt et al., 2006a, b) aboard the sun-synchronous EOS Aura satellite was launched in July 2004. It achieves daily global coverage with a spatial resolution of 24 × 13 km^2 in nadir and about 150 × 13 km^2 at the swath edges (Levelt et al., 2006b). The overpass time is around 13:30 LT. In this study, we validate the operational level 2 (Boersma et al., 2007, 2011) tropospheric NO$_2$ VCD (DOMINO version 2) obtained from the TEMIS website (http://www.temis.nl). The NO$_2$ SCDs are retrieved in the 405–465 nm spectral window using a DOAS algorithm and are converted to NO$_2$ tropospheric VCDs using tropospheric AMFs from a look-up table, which is generated using the DAK RTM (Stammes, 1994), after the stratospheric column was subtracted. SFs of NO$_2$ for the AMF calculations are obtained from the TM4 CTM (Williams et al., 2009) for individual measurements and can be downloaded from the TEMIS website. TM4 assimilations run at a resolution of 2° × 3° (latitude × longitude) and 35 vertical levels up to 0.38 hPa, and are spatially interpolated to the OMI pixel centre (Boersma et al., 2007, 2011; Dirksen et al., 2011). The effective cloud fraction (eCF) (Stammes et al., 2008; Wang et al., 2008) and cloud top pressure (CTP) (Acarreta et al., 2004) are obtained from the OMCLDO2 cloud product based

on the O$_4$ absorption band at 477 nm assuming a Lambertian cloud with an albedo of 0.8. The retrieval algorithm for DOMINO v2 forms the basis of NO$_2$ retrievals for the upcoming Tropospheric Monitoring Instrument (TROPOMI) aboard the Sentinel-5 Precursor mission (Veefkind et al., 2012).

Two data sets of tropospheric SO$_2$ VCDs derived from OMI observations are validated in this study. One is the operational level 2 OMSO2 planetary boundary layer (PBL) SO$_2$ data set (assuming SO$_2$ mostly in the PBL) provided via the NASA website (http://avdc.gsfc.nasa.gov). In the following this product is simply referred to as "OMI NASA". For the PBL SO$_2$ product, the VCD is derived from the measured radiances of the OMI instrument between 310.5 and 340 nm using a principal component analysis (PCA) algorithm (C. Li et al., 2013). A fixed surface albedo (0.05), surface pressure (1013.25 hPa), solar zenith angle (30°) and viewing zenith angle (0°) as well as a fixed climatological SO$_2$ profile over the summertime eastern US are assumed in the PCA retrieval (Krotkov et al., 2008). The second product is derived by a new OMI SO$_2$ retrieval algorithm developed by BIRA (Theys et al., 2015). In the following this product is simply referred to as "OMI BIRA". It forms the basis of the algorithm for the operational level-2 SO$_2$ product to be derived from the upcoming TROPOMI instrument. SO$_2$ SCDs are first retrieved in a window between 312 and 326 nm using the DOAS technique and then a background correction for possible biases is applied. The SO$_2$ SCDs are converted to VCDs using AMFs from a look-up table, which is generated using the Linearized Discrete Ordinate Radiative Transfer (LIDORT) version 3.3 RTM (Spurr et al., 2001, 2008). SFs for SO$_2$ are obtained from the IMAGES CTM (Müller and Brasseur, 1995) for individual measurements at a horizontal resolution of 2° × 2.5° and at 40 vertical unevenly distributed levels extending from the surface to the lower stratosphere (44 hPa) (Stavrakou et al., 2013, 2015). Like for the OMSO2 data set, the cloud information is obtained from the OMCLDO2 cloud product.

The HCHO data set validated in this study is the OMI HCHO tropospheric VCD level 2 data retrieved by a DOAS algorithm v14 developed at BIRA-IASB (De Smedt et al., 2015). This algorithm will also be applied to the upcoming TROPOMI instrument. HCHO SCDs are retrieved in the spectral window between 328.5 and 346 nm using the DOAS technique. After applying a background correction, HCHO SCDs are converted to tropospheric VCDs using AMFs from a look-up table generated by LIDORT with HCHO SFs obtained from the IMAGES CTM for individual measurements (Stavrakou et al., 2015). Also, for this product the cloud information is obtained from the OMCLDO2 cloud product.

Here one important aspect should be noted: different AMF strategies are used in the DOMINO v2 NO$_2$ product and the BIRA SO$_2$ and HCHO products for eCF < 10 %. For the NO$_2$ product the eCF and CTP are explicitly considered in the AMF simulations while for the SO$_2$ and HCHO

products the clear-sky AMFs are applied. These differences will be especially important for measurements in the presence of high aerosol loads (see Sect. 3.5). For eCF > 10 %, a cloud correction based on the independent pixel approximation (IPA) (Cahalan et al., 1994) is applied for the three TG retrievals. It should also be noted that observations of the outermost pixels (i.e. pixel numbers 1–5 and 56–60) and pixels affected by the so-called "row anomaly" (see http://www.temis.nl/airpollution/no2col/warning.html) were removed before the comparisons.

2.3 NO$_2$, SO$_2$ and HCHO products derived from GOME-2

The GOME-2A and B instruments (Callies et al., 2000; Munro et al., 2006, 2016) are aboard the sun-synchronous Meteorological Operational Satellite platforms MetOp-A and MetOp-B, respectively. MetOp-A (launched on 19 October 2006) and MetOp-B (launched on 17 September 2012) operate in parallel with the same equator crossing time of 09:30 LT. Before 15 July 2013 GOME-2A had a swath width of 1920 km, corresponding to a ground pixel size of 80 km × 40 km and a global coverage within 1.5 days. Since 15 July 2013, the GOME-2A swath width was changed to 960 km with a ground pixel size of 40 km × 40 km. The GOME-2A settings before 2013 are also applied to GOME-2B.

In this study, we validate the operational level 2 tropospheric NO$_2$ VCDs derived from the TM4NO2A version 2.3 product (Boersma et al., 2004) for GOME-2A and B obtained from the TEMIS website. The NO$_2$ SCDs are retrieved in the 425–450 nm spectral window by the BIRA team with QDOAS (http://uv-vis.aeronomie.be/software/QDOAS/). The tropospheric NO$_2$ VCDs are obtained from the SCDs using similar data assimilation procedures as for the DOMINO v2 product. However, for the GOME-2 products the eCF and CTP are retrieved by the improved Fast Retrieval Scheme for Clouds from the Oxygen A-band algorithm (FRESCO+) based on the measurements of the oxygen A-band around 760 nm (Wang et al., 2008), again assuming a Lambertian cloud.

Two SO$_2$ products derived from GOME-2A observations are included in the study. The first one is the operational level 2 O3M-SAF SO$_2$ product derived from GOME-2A observations (Rix et al., 2012; Hassinen et al., 2016). In the following the product is simply referred to as "GOME-2A DLR". This product is provided via the EUMETSAT product navigator (http://navigator.eumetsat.int) or the DLR EOWEB system (http://eoweb.dlr.de). The SO$_2$ SCDs are retrieved using the DOAS technique in the wavelength range between 315 and 326 nm. For the conversion of SCDs to VCDs, the AMFs are acquired from a look-up table generated using LIDORT 3.3. For the AMF computation, three types of SFs are assumed as Gaussian distributions with a FWHM of 1.5 km around three central heights of 2.5, 6 and 15 km. Because for

the SO$_2$ concentrations at Wuxi mostly anthropogenic pollution is relevant, only the SO$_2$ product corresponding to the central height of 2.5 km is included in the validation study. The cloud information is obtained from GOME-2 measurements by the OCRA and ROCINN algorithms (Loyola et al., 2007) based on oxygen A-band observations at around 760 nm. The second product is provided by BIRA using the same retrieval algorithm as for the OMI BIRA SO$_2$ product, referred to as "GOME-2A BIRA". The same algorithm is also used to acquire the SO$_2$ data from GOME-2B observations. The product is referred to as "GOME-2B BIRA" in the following. The cloud properties used in the two products are derived from GOME-2A/B observations using the FRESCO+ algorithm.

The HCHO tropospheric VCD level 2 products derived from GOME-2A and B observations (De Smedt et al., 2012, 2015) are validated in this study. The same retrieval approach as for the OMI BIRA HCHO product is applied, but the cloud properties are derived from GOME-2A/B observations using the FRESCO+ algorithm.

3 Validation of the satellite data sets

In this section the daily and bi-monthly-averaged NO$_2$, SO$_2$ and HCHO VCDs from OMI and GOME-2 are validated by comparisons with the tropospheric VCDs derived from the MAX-DOAS observations. Here it needs to be clarified that the daily and bi-monthly satellite data are the averaged values of all satellite pixels located in the coincidence area around the measurement site (see below). The MAX-DOAS data are the averaged values for all measurements within 2 h around the satellite overpass time. Also, the diurnal and weekly cycles from the satellite observations are compared with those from the corresponding MAX-DOAS observations. Finally the influence of the SF and the effects of aerosols on the OMI products are discussed. The SFs from the CTM used for the OMI AMF calculations are compared to the SFs derived from MAX-DOAS.

Averaging of individual satellite and/or MAX-DOAS observations can be advantageous for several reasons. First, especially for observations with rather large statistical uncertainties (in particular for satellite observations of SO$_2$ and HCHO), the merging of several observations can substantially reduce these uncertainties. Second, the effect of spatial gradients across satellite pixels can be partly accounted for by averaging MAX-DOAS measurements over a period around the satellite overpass time. However, for the averaging of satellite and MAX-DOAS data, reasonable selection criteria need to be determined, which can be different for the different TGs and satellite sensors. The effects of the selection criteria, in particular the time period used for the MAX-DOAS measurements and the distance of the selected satellite observations from the measurement site are evaluated and discussed in detail in Sect. S1 in the Supplement. One general

finding is that the effect of the chosen time period is negligible compared to the effect of the chosen distance. Therefore it is reasonable to arbitrarily use 2 h around the satellite overpass time, namely 12:30 to 14:30 LT for the comparisons with OMI and from 08:30 to 10:30 LT for the comparisons with GOME-2A/B. The distances around the measurement site, for which satellite observations are averaged, are chosen differently for the different satellite products based on the sensitivity studies shown in Sect. S1. In the following comparisons, the OMI NO$_2$ and SO$_2$ (HCHO) data are selected for satellite pixels with distances < 20 km (< 50 km) from the Wuxi station. The GOME-2A/B data of the three species are selected for distances < 50 km. It should be noted that these findings are derived for a polluted site in China. For other locations and conditions, different coincidence criteria might be best suited.

3.1 Daily comparisons

The daily-averaged satellite data for measurements within the chosen distances are compared with the daily-averaged MAX-DOAS data within 2 h around the satellite overpass time. To characterize the cloud effect on the comparisons, the comparisons are performed for different eCF bins of 0–10, 10–20, 20–30, 30–40, 40–50 and 50–100 % for NO$_2$ and SO$_2$, and for eCF bins of 0–10, 10–30, 30–50 and 50–100 % for HCHO. Note that the cloud effects on the MAX-DOAS results are discussed in detail in Sect. S2. The most important finding is that the cloud effects on MAX-DOAS results are negligible for the satellite validation activities.

3.1.1 NO$_2$

Figure 2a, b and c display scatter plots (and the parameters from the linear regressions) of the daily-averaged NO$_2$ tropospheric VCDs derived from OMI, GOME-2A and GOME-2B products versus those derived from the corresponding MAX-DOAS measurements for eCF < 10 %. Generally higher correlation coefficients (R^2) are found for OMI than for GOME-2A/B. The systematic biases of the satellite data with respect to the MAX-DOAS data are quantified by the mean relative difference (MRD) calculated following Eq. (1):

$$\text{MRD} = \frac{\sum_1^n (V_{s_i} - V_{M_i})/V_{M_i}}{n}. \tag{1}$$

Here V_{s_i} and V_{M_i} represent the averaged TG VCDs from satellite observations and MAX-DOAS measurements on day i, respectively; n is the total number of the available days. The MRD is only 1 % for OMI, and 27 and 30 % for GOME-2A and B, respectively.

The R^2, slopes and intercepts of the linear regressions and the MRD, as well as the number of available days for the three satellite products, are shown for the five eCF bins in Fig. 3. For OMI, R^2 decreases with increasing eCF; the slopes significantly change for eCF > 50 % and the
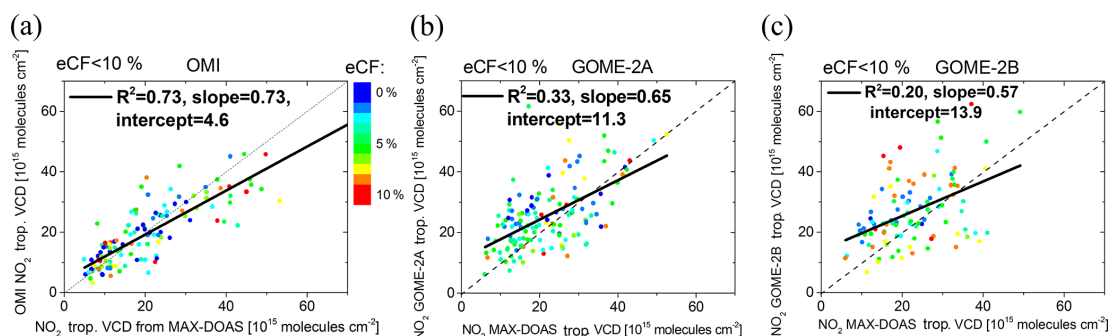
Figure 2. Daily-averaged NO$_2$ tropospheric VCDs derived from OMI **(a)**, GOME-2A **(b)** and GOME-2B **(c)** compared with the corresponding MAX-DOAS data for eCF < 10 %. The colours indicate the eCF.
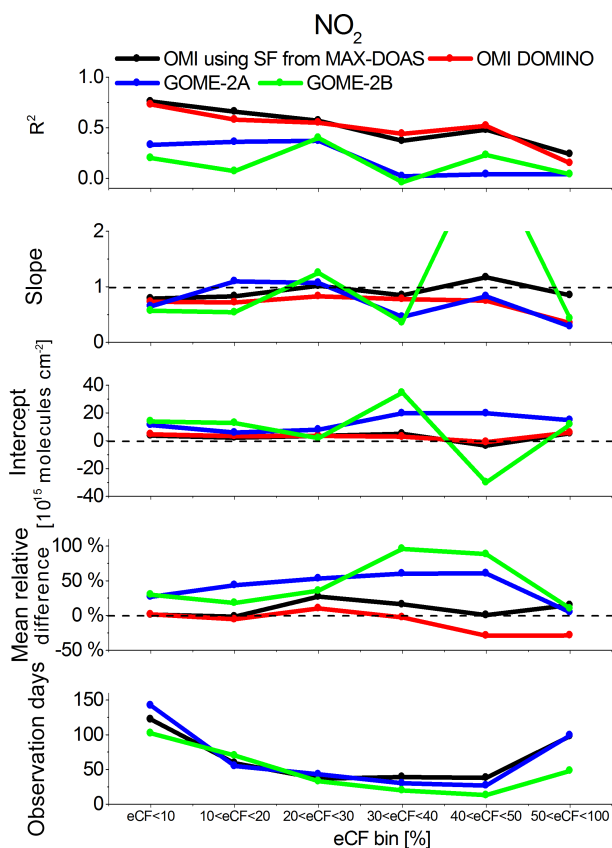

Figure 3. R^2, slopes, intercepts, mean relative differences (and the number of available days) derived from the comparisons of the NO$_2$ VCDs from different satellite instruments to the MAX-DOAS results for the different eCF bins. Note that the black and red curves represent the improved OMI VCDs with the a priori shape factors derived from Wuxi MAX-DOAS observations (see Sect. 3.2) and for the DOMINO 2 product, respectively.

MRD drops to −40 % for eCF > 40 %. For GOME-2A, a steep decrease of R^2 for eCF > 30 % is found. For GOME-2B, a generally lower R^2 is found for eCF > 30 %; the MRD indicates an increasing systematic overestimation for

eCF > 30 %. Thus we conclude that the cloud effect on OMI and GOME-2A/B NO$_2$ data becomes significant for eCF > 40 and 30 %, respectively.

3.1.2 SO$_2$

Figure 4a, b, c, d, and e display scatter plots of the daily-averaged SO$_2$ tropospheric VCDs derived from the OMI NASA, OMI BIRA, GOME-2A DLR, GOME-2A and B BIRA products versus those derived from the corresponding MAX-DOAS measurements for eCF < 10 %. R^2 and slopes are more close to unity for the OMI BIRA product than for the other products. The MRDs indicate a similar systematic underestimation (−40 to −52 %) by all products. There are fewer negative values in the OMI BIRA product than in the other satellite products. It needs to be noted that the significantly worse R^2 for the OMI NASA product compared to the OMI BIRA product could partly be attributed to the assumed fixed measurement condition (and thus the fixed AMF) in the NASA PCA retrievals. However, the similar slopes and MRDs between the two OMI products indicate that the simplification of the NASA PCA retrieval only slightly contributes to the systematic bias of the averaged values.

The R^2, slopes and intercepts of the linear regressions and the MRD, as well as the number of the available days obtained for the five satellite SO$_2$ products, are shown for the five eCF bins in Fig. 5. For the OMI BIRA product, a significant decrease of R^2 occurs for eCF > 10 % together with a decrease of the slopes and the MRD. A steep increase of the MRD is found for eCF > 40 %. Therefore cloud effects on the OMI BIRA SO$_2$ data become considerable for eCF > 10 %. For the OMI SO$_2$ NASA data, R^2, slope, and MRD significantly decrease for eCF > 20 %. R^2 for both GOME-2A data are low (< 0.09) for all eCF bins; thus from the linear regressions no meaningful information on the cloud effect can be derived. Almost constant MRDs are found for both GOME-2A SO$_2$ products for eCF < 30 %. For eCF > 30 % largely varying MRD are found, especially for the GOME-2A BIRA products. Thus we conclude that the cloud effects on both GOME-2A products are appreciable for eCF > 30 %. For the
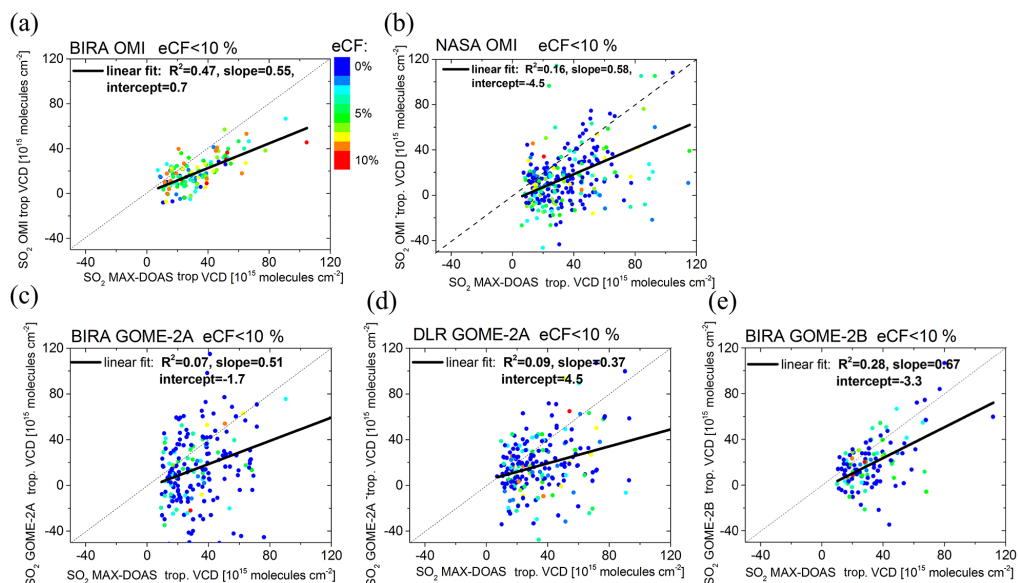
Figure 4. Daily-averaged OMI SO$_2$ tropospheric VCDs from BIRA **(a)** and NASA **(b)**, GOME -2A SO$_2$ tropospheric VCDs from BIRA **(c)** and DLR **(d)**, and GOME-2B SO$_2$ tropospheric VCDs from BIRA **(e)** for eCF < 10 % plotted versus the coincident MAX-DOAS results. The colours indicate the eCF.

GOME-2B BIRA data, an obvious decrease of R^2 and slope is found for eCF > 10 %, while for eCF > 30 % largely variable MRDs are found. Thus clouds can considerably impact the GOME-2B BIRA product for eCF > 10 %, and more significantly for eCF > 30 %.

3.1.3   HCHO

Because of the rather small atmospheric absorption of HCHO, the DOAS fit errors often dominate the total uncertainty of the HCHO satellite data (De Smedt et al., 2015). Thus systematic effects (e.g. those caused by clouds) are more difficult to identify and quantify than for NO$_2$ and SO$_2$. The scatter plot of the OMI HCHO VCDs for individual pixels versus those derived from MAX-DOAS observations for eCF < 30 % are shown in Fig. 6. One important finding is that the R^2 for data with a fit error $< 7 \times 10^{15}$ molecules cm^{-2} is better than the R^2 for all data (see Fig. 6b). A similar result is obtained for the daily-averaged OMI HCHO VCDs (see Fig. S12 in the Supplement) indicating that the fit error dominates the random uncertainty of the HCHO VCDs derived from satellite. In contrast, the slopes of the linear regressions for the OMI data before and after the filtering are quite similar, as shown in Figs. 6b and S12. Thus the data screening has no considerable impact on the analysis of the systematic bias of the OMI HCHO products. Considering that the mean fit error of the HCHO VCDs is 7×10^{15} molecules cm^{-2} for the OMI data, for further comparisons we exclude the HCHO VCDs with fit errors $> 7 \times 10^{15}$ molecules cm^{-2} for OMI. However, for the GOME-2A/B products, the filter for the fit error is not applied because in contrast to the OMI HCHO
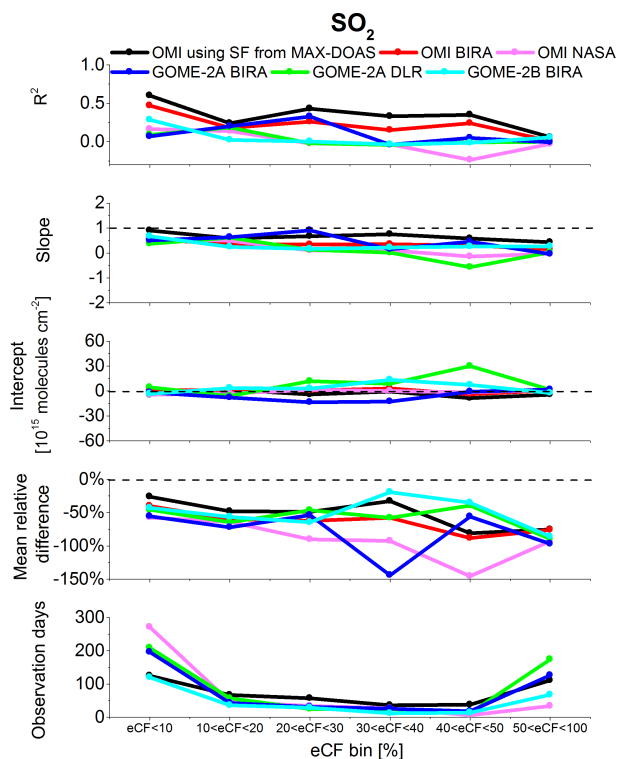

Figure 5. Same as Fig. 3 but for SO$_2$.

data we find a systematic dependence of the fit error on the retrieved HCHO tropospheric VCD (see Fig. S13). The different findings with respect to the HCHO fit error for OMI
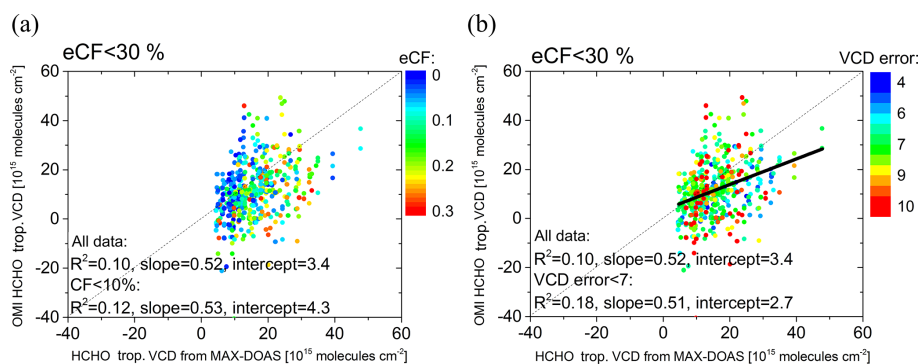
Figure 6. (a) HCHO tropospheric VCDs for OMI pixels for eCF < 30 % are plotted against those derived from MAX-DOAS observations with the colour map of eCF; the linear regression parameters are acquired for eCF < 30 % and for eCF < 10 %, respectively. **(b)** Scatter plots are same as in **(a)**, but with the colour map of VCD fit error; linear regression parameters are acquired for all data and for VCD fit error < 7 × 10^{15} molecules cm^{-2}.

and GOME-2 are not clearly understood and should be addressed in further investigations.

If the additional filter of the fit error for the OMI product is applied, 48 % of the total number of HCHO data is left for comparisons. In order to still include a sufficient number of data, we use broader eCF bins (0–10, 10–30, 30–50 and 50–100 %). Figure 7a, c and d display scatter plots of the satellite daily-averaged data versus the MAX-DOAS data for eCF < 10 % for OMI, GOME-2A and GOME-2B data, respectively. We found the best consistency for the GOME-2B product, probably because of the weaker degradation of GOME-2B during the short time after launch compared to OMI and GOME-2A. Nevertheless, other unknown reasons might also play a role. One interesting finding is the better correlation of the OMI products for the eCF bin of 10 to 30 % (see Fig. 7b) compared to the eCF < 10 %. However, for eCF of 10 to 30 % also a larger MRD of −34 % (see Fig. 8) is found, which might be attributed to the effect of clouds, because the clear-sky AMFs used in the retrievals for eCF < 10 % (see the last paragraph of Sect. 2.2).

The dependencies of the results of the linear regressions and the MRDs on the eCFs are shown in Fig. 8 for the three satellite instruments. For OMI, a decrease of R^2 occurs for eCF > 30 %, while for GOME-2A and GOME-2B, low R^2 are already found for eCF > 10 %. Gradually increasing absolute values of the MRDs for all satellite instruments are found for increasing eCF. In general cloud effects on the HCHO products become substantial for eCF > 30 % for the three satellite instruments. However, it needs to be noted that our findings are derived for one location (Wuxi) and might not be fully representative for other locations. The use of the HCHO products with eCF < 40 % is recommended by the retrieval algorithm developer (De Smedt et al., 2015).

3.2 Errors of shape factors from CTM and the effect on satellite VCD products

The SF is an input for the calculation of satellite AMF, which is needed to convert the SCD to the VCD (Palmer et al., 2001). Different retrieval algorithms acquire the SFs in different ways, mostly from a CTM for individual measurements or assuming a fixed SF (see Sect. 2.2 and 2.3). The MAX-DOAS measurements acquire the vertical profiles of NO$_2$, SO$_2$ and HCHO from the ground up to the altitude of about 4 km (depending on the measurement conditions), in which the tropospheric amounts of the TGs are mostly located. Thus the profiles derived from MAX-DOAS observations are valuable to evaluate the SFs used in the satellite retrievals and their effects on the AMFs and VCDs. Because the averaging kernels and SFs for individual satellite measurements are available only for the DOMINO NO$_2$, BIRA SO$_2$, and BIRA HCHO products derived from OMI observations, these three products are used to evaluate the effect of the SF in this section.

For the three selected products, the calculation of the tropospheric satellite AMFs follows the same way as introduced in Palmer et al. (2001) as Eq. (2):

$$\text{AMF} = \int_{\text{ground}}^{\text{tropopause}} \text{BAMF}(z)\text{SF}(z)\text{d}z. \tag{2}$$

Here BAMF(z) is the box AMF, which characterizes the measurement sensitivity as a function of altitude (z). The integration is done from the ground to the tropopause. The SFs of the TGs are obtained from different CTM (TM4 for NO$_2$, IMAGES for SO$_2$ and HCHO, see Sect. 2.2). The profiles (profile$_\text{M}$) derived from MAX-DOAS can be converted to SF (SF$_\text{M}$) using Eq. (3):

$$\text{SF}_\text{M}(z) = \frac{\text{profile}_\text{M}(z)}{\text{VCD}_\text{M}}, \tag{3}$$
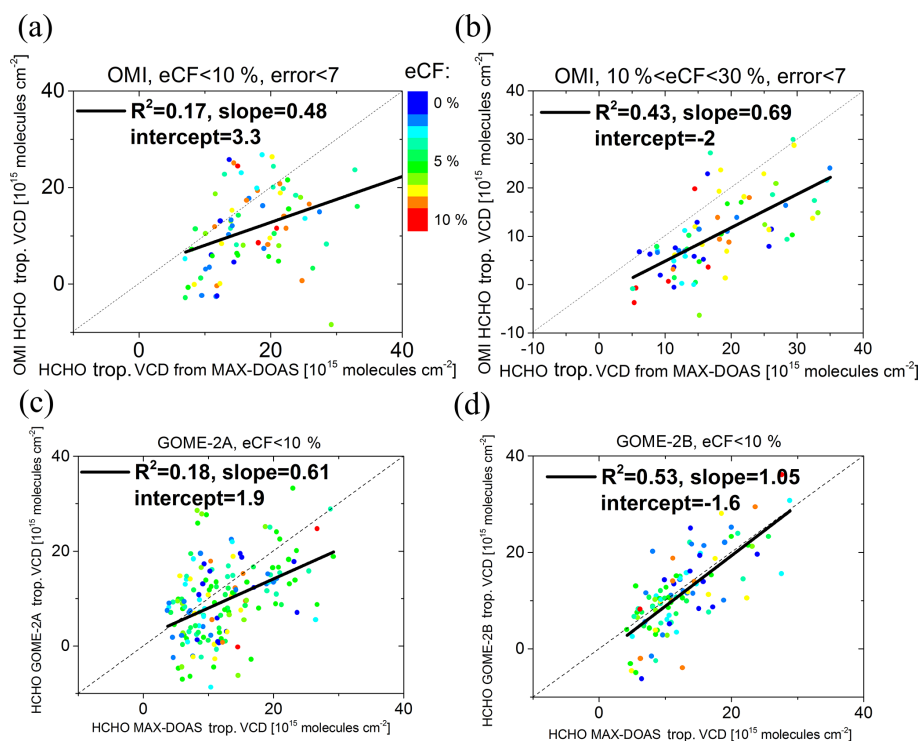
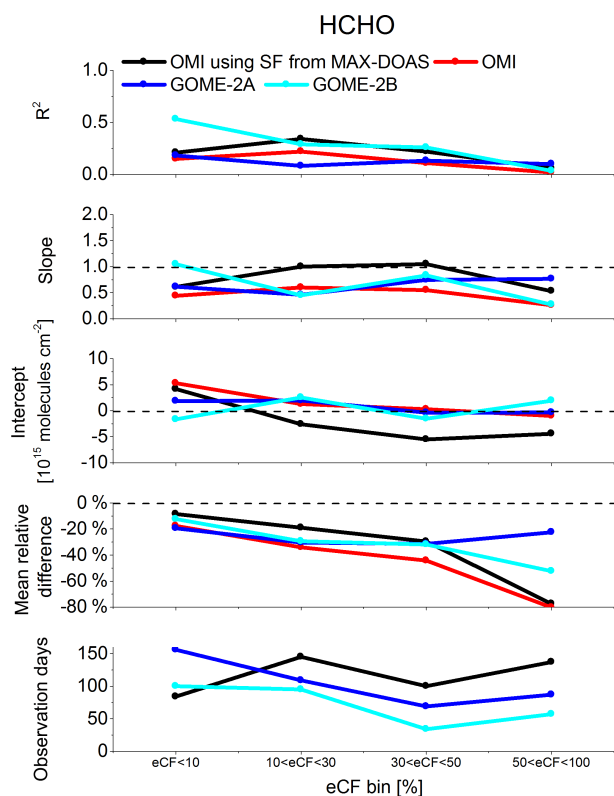**Figure 7.** Same as Fig.2, but for HCHO.

Figure 8. Same as Fig. 3 but for HCHO.

where VCD$_M$ is the tropospheric VCD derived by an integration of the corresponding profile$_M$. It needs to be noted that only the profiles below 4 km can be reliably drawn from MAX-DOAS observations. Thus the profile$_M$ between 4 km and the tropopause (a fixed value of 16 km is used in this study) is derived from the corresponding CTM profiles of the individual satellite data sets. Therefore the SF$_M$ is derived from the combined profile$_M$ using Eq. (3).

A similar relationship connects the BAMFs and averaging kernels (Eskes and Boersma, 2003):

$$AK(z) = \frac{BAMF(z)}{AMF}. \tag{4}$$

The SF$_M$ can replace the SF from CTM (SF$_C$) to recalculate the AMF using Eq. (2). A similar study was recently conducted by Theys et al. (2015) and De Smedt et al. (2015) for the OMI BIRA SO$_2$ and HCHO products over the Xianghe area. They demonstrated the improvements of the consistency between OMI VCDs and MAX-DOAS VCDs when using the SF$_M$ for the AMF calculation of the satellite products by 20–50 %. In our study we follow the same procedure.

3.2.1   NO$_2$

The averaged NO$_2$ SF$_C$ for the measurements under clear sky with eCF < 10 % is compared to SF$_M$ in the altitude range of up to 4 km in Fig. 9a. The differences between the averaged SF$_C$ and SF$_M$ shown in Fig. 9b indicate that in the layer below 4 km NO$_2$ SF$_C$ is considerably larger than SF$_M$ below
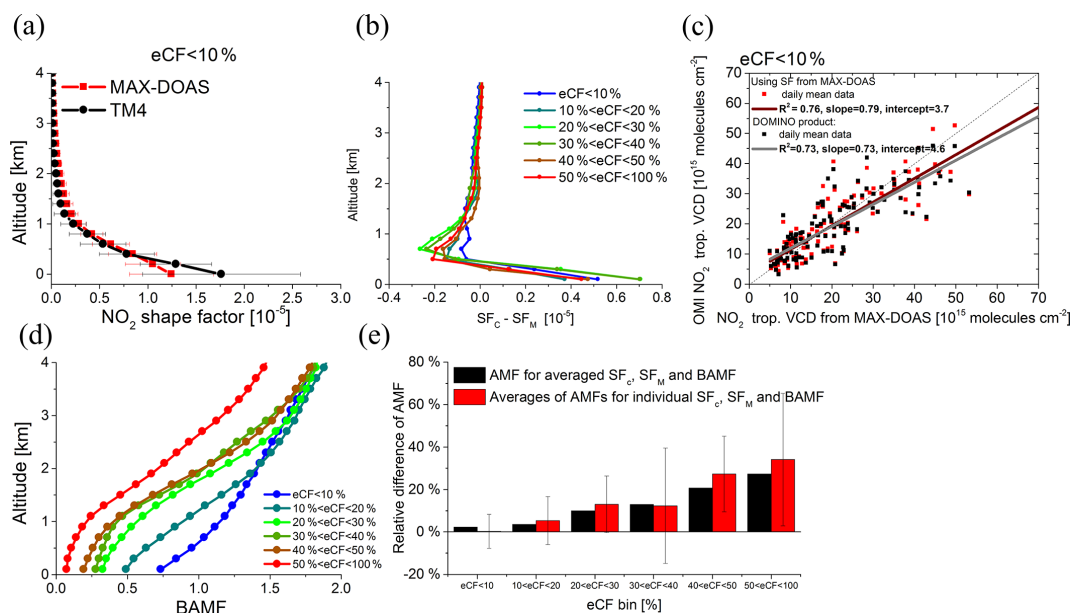
Figure 9. (a) Average NO$_2$ SFs and standard deviations derived from the MAX-DOAS observations and from the TM4 CTM (for the DOMINO product) for eCF < 10 %. **(b)** Averaged differences between the NO$_2$ SFs from CTM (SF$_C$) and from MAX-DOAS (SF$_M$) for different eCF bins. **(c)** Daily averages of the original DOMINO NO$_2$ product and modified NO$_2$ product (based on MAX-DOAS SF) plotted against those from MAX-DOAS for eCF < 10 %. **(d)** Averaged BAMF for satellite observation for different eCF bins. **(e)** Relative difference (RD) of satellite AMF using SF$_C$ (AMF$_{CTM}$) or SF$_M$ (AMF$_{MAX-DOAS}$) for different eCF bins. The error bars indicate the standard deviation of the RDs for each eCF bin. Black columns denote the RDs derived from the averaged SF$_C$, SF$_M$ and BAMF (shown in **b** and **d**); red columns denote the averaged RDs for individual SF$_C$, SF$_M$ and BAMF of each satellite observation.

0.4 km and smaller above 0.4 km. In the altitude range above 4 km, SF$_C$ is slightly larger than SF$_M$ (see Fig. S14a). The OMI VCDs (VCD$_{CTM}$) retrieved with SF$_C$ (directly derived from the DOMINO NO$_2$ product) and the modified OMI VCDs (VCD$_{SM}$) (based on SF$_M$ and the NO$_2$ SCDs which are derived from the DOMINO NO$_2$ product) are plotted against the VCDs derived from MAX-DOAS observations in Fig. 9c. Very similar results for both VCD$_{CTM}$ and VCD$_{SM}$ are found. In Fig. 9e the relative differences of the AMFs using either SF$_C$ (AMF$_{CTM}$) or SF$_M$ (AMF$_{MAX-DOAS}$) are shown. The differences are calculated in two ways: either the relative differences are first calculated for individual measurements, and then the individual relative differences are averaged. Alternatively, first the AMFs of the individual measurements are averaged, and then the relative differences are calculated. The results in Fig. 9e show that for both calculations very similar results are also obtained. For eCF < 10 % the relative differences are only 0.3 %. The small differences can be explained by a compensation effect of the negative and positive differences between SF$_C$ and SF$_M$ near the surface and at high altitudes, respectively.

For different eCF bins, the relative differences of AMF$_{CTM}$ and AMF$_{MAX-DOAS}$ increase systematically with increasing eCF. This finding can be explained by the partial AMF above 4 km (see Fig. S14c). The partial AMF$_{CTM}$ is always larger than the partial AMF$_{MAX-DOAS}$ above 4 km

because SF$_C$ is larger than SF$_M$. And the difference increases substantially with increasing eCF. Meanwhile the contribution of the partial AMF above 4 km to the total tropospheric AMF increases with increasing eCF due to the strong decrease of the partial AMF below. Overall the overestimation of the partial AMF$_{CTM}$ compared to the partial AMF$_{MAX-DOAS}$ above 4 km becomes critical under cloudy conditions.

In general the TM4 NO$_2$ a priori profile shapes agree well with the MAX-DOAS profiles, and the agreement with the MAX-DOAS VCDs by replacing SF$_C$ with SF$_M$ in the AMF calculation is only slightly improved for a small eCF. For large eCF, VCD$_{SM}$ is systematically larger than VCD$_{CTM}$ by 20 % on average (see Fig. 3), consistent with the AMF differences shown in Fig. 9e.

3.2.2 SO$_2$

The results shown in Fig. 10a and b indicate that in the layer below 4 km for eCF < 10 %, the SO$_2$SF$_C$ is considerably smaller than SF$_M$ below 1 km and larger above 1 km, respectively. As can be seen in Fig. S15a, SF$_C$ is in general slightly larger than SF$_M$ in the altitude range above 4 km. Since the BAMFs increase with altitude (Fig. 10d) SO$_2$AMF$_{CTM}$ are on average larger than AMF$_{MAX-DOAS}$ by 18 % (Fig. 10e). In contrast to NO$_2$, the SO$_2$ VCD$_{SM}$ agrees better with the MAX-DOAS VCDs than VCD$_{CTM}$, i.e. R^2 and slope in-
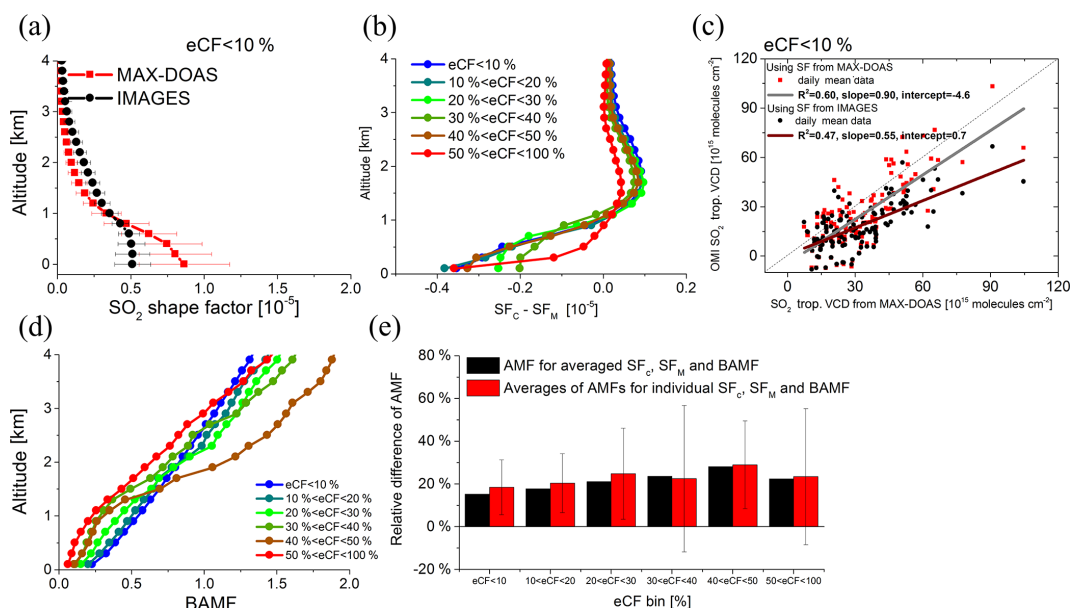
Figure 10. Similar to Fig. 9 but for the OMI BIRA SO$_2$ product. Note that the SF for the OMI BIRA product is obtained from the IMAGES CTM.

crease from 0.47 to 0.60 and from 0.55 to 0.90, respectively (see Fig. 10c). Also, the systematic bias of VCD$_{SM}$ is smaller than that of VCD$_{CTM}$, i.e. the MRD is −26 % for VCD$_{SM}$ and −40 % for VCD$_{CTM}$ (see black and red curves in Fig. 5).

For different eCF bins, the differences between SO$_2$SF$_C$ and SF$_M$ (Fig. 10b) as well as BAMFs (Fig. 10d) are slightly different from each other in the altitude range below 4 km. However, an obvious dependence of both quantities above 4 km on eCF can be seen in Fig. S15a and b. The overestimation of SF$_C$ compared to SF$_M$ above 4 km increases with increasing eCF, and the BAMF above 4 km also increases with increasing eCF. Therefore the dependences of both quantities on eCF dominates the different levels of agreement of the partial AMF$_{CTM}$ and partial AMF$_{MAX-DOAS}$ above 4 km for different cloud conditions, as shown in Fig. S15c. Furthermore, the partial AMF above 4 km dominates the total tropospheric AMF for large eCF due to the decrease of the lower partial AMF with increasing eCF (see Fig. S15c). These dependencies of partial AMF$_{CTM}$ and partial AMF$_{MAX-DOAS}$ above 4 km on eCF also explain the dependencies of differences between the total tropospheric AMF$_{CTM}$ and AMF$_{MAX-DOAS}$ on eCF, as shown in Fig. 10e. However, in general the dependences on eCF are smaller than that for NO$_2$. In addition, a better consistency between the SO$_2$ VCD$_{SM}$ and the MAX-DOAS VCDs than for the VCD$_{CTM}$ can be seen in Fig. 5 for all the eCF bins.

3.2.3   HCHO

The results shown in Fig. 11a and b indicate that in the altitude range below 4 km for eCF < 10 % the HCHO SF$_C$ is considerably smaller below 1.7 km and larger than SF$_M$ above

1.7 km, respectively. As can be seen in Fig. S16a, the SF$_C$ almost equals the SF$_M$ above 4 km for eCF < 10 %. Since the BAMF increases with altitude (Fig. 11d) the HCHO AMF$_{CTM}$ is on average larger than AMF$_{MAX-DOAS}$ by 11 % (Fig. 11e). Like for SO$_2$ the VCD$_{SM}$ agree better with the MAX-DOAS VCD than VCD$_{CTM}$, i.e. R^2 and slope increase from 0.15 to 0.21 and from 0.44 to 0.61, respectively (see Fig. 11c). Also, the systematic bias of VCD$_{SM}$ is smaller than that of VCD$_{CTM}$, i.e. the MRD is −10 % for VCD$_{SM}$ and −18 % for VCD$_{CTM}$ (see Fig. 8).

For different eCF bins, larger differences between AMF$_{CTM}$ and AMF$_{MAX-DOAS}$ are found towards larger eCF (see Fig. 11e). Similar to NO$_2$ and SO$_2$, this finding is caused by the partial AMFs above 4 km. The dependences of differences between HCHO SF$_C$ and SF$_M$ (Fig. 11b) as well as BAMFs (Fig. 11d) in the altitude range below 4 km on eCF are insignificant. However, both quantities above 4 km obviously depend on eCF (see Fig. S16a and b). The overestimation of SF$_C$ compared to SF$_M$ above 4 km increases with increasing eCF, and the BAMF above 4 km also increases with increasing eCF. Therefore the dependences of both quantities on eCF dominate the different levels of agreement of the partial AMF$_{CTM}$ and partial AMF$_{MAX-DOAS}$ above 4 km for different cloud conditions, as shown in Fig. S16c. Furthermore, the partial AMF above 4 km dominates the total tropospheric AMF for large eCF due to the decrease of the partial below-4 km AMF with increasing eCF (see Fig. S16c). These dependencies of partial AMF$_{CTM}$ and partial AMF$_{MAX-DOAS}$ above 4 km on eCF also explain the dependencies of differences between the total tropospheric AMF$_{CTM}$ and AMF$_{MAX-DOAS}$ on eCF, as shown in Fig. 11e.
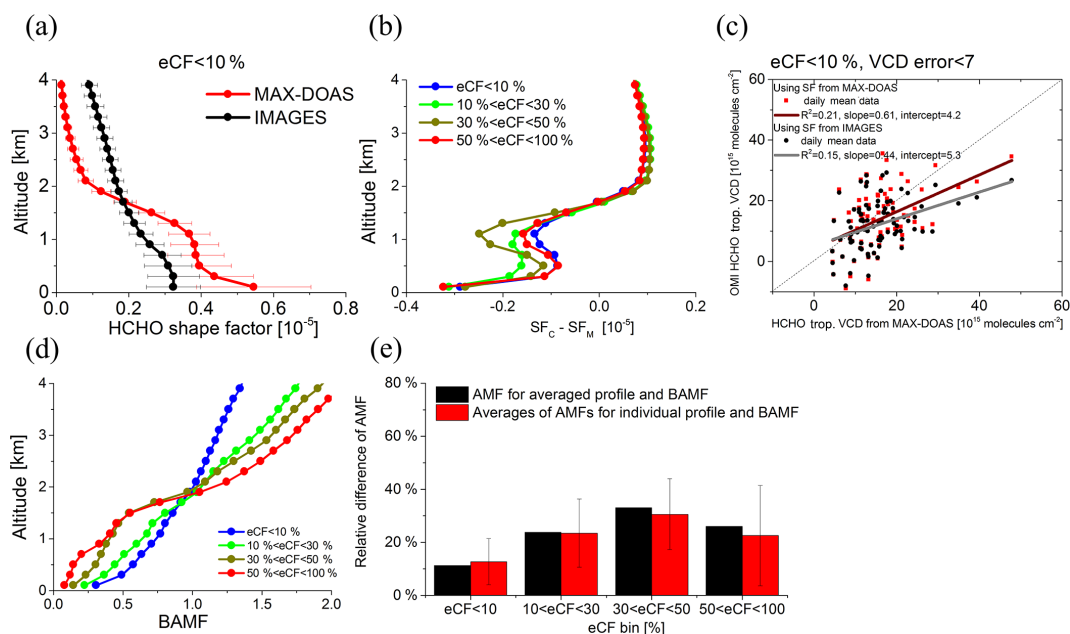
Figure 11. Same as Fig. 9 but for the OMI BIRA HCHO product and eCF bins of 0–10, 10–30, 30–50 and 50–100 %. Note that the SF for the OMI BIRA product is obtained from the IMAGES CTM.

In addition, Fig. 8 shows that for all the eCF bins the consistency between VCD_{SM} and the MAX-DOAS VCD is better than for VCD_{CTM}.

3.2.4 Uncertainties of the SF from MAX-DOAS

The previous study on the Wuxi MAX-DOAS observations (Wang et al., 2017) demonstrated that in general the profile retrievals are not sensitive to altitudes above 1–2 km, where the retrieved profiles are strongly constrained to the a priori profiles. Thus the SFs at high altitudes could be underestimated by MAX-DOAS retrievals. This effect could be considerable, especially for SO_2 and HCHO, because they typically extend to higher altitudes than NO_2 (Xue et al., 2010; Junkermann, 2009; Wagner et al., 2011). Because BAMFs of satellite observations are normally larger at high altitudes, the uncertainties of SFs from MAX-DOAS could cause an underestimation of $AMF_{MAX-DOAS}$, which further could cause an overestimation of VCD_{SM}. Since the profiles above 4 km are not available from MAX-DOAS observation, they are taken from the corresponding CTM simulations for the different satellite data sets in this study. This procedure can contribute to an unknown error in the analysis of SF effects on satellite AMF and VCD calculations.

3.3 Comparisons of the bi-monthly mean VCD

We calculate bi-monthly-averaged tropospheric VCDs for eCF < 30 % for the coincident observations of the satellite instruments and MAX-DOAS (and also from the CTM simulations for the OMI products) from 2011 to 2014. The results

for NO_2, SO_2 and HCHO are shown in Fig. 12. The numbers of available days for each satellite product are also shown in the bottom panels of each subfigure.

3.3.1 NO_2

For OMI, good agreements with the MAX-DOAS VCDs are found both for the DOMINO and the improved VCDs using SFs from MAX-DOAS observations with a slightly better agreement for the improved VCDs. GOME-2A and B VCDs are systematically larger than the MAX-DOAS VCDs by about 5×10^{15} molecules cm^{-2} on average. The overestimation could be attributed to the errors of the NO_2 SFs from TM4 (Pinardi et al., 2013). Systematic differences between the GOME2-A and B VCDs are found, which can be partly explained by the different swath widths of both sensors after 15 July 2013. For the same reason, better agreement between GOME-2A and MAX-DOAS VCDs is also found after summer 2013. The NO_2 VCDs simulated by TM4 for the OMI DOMINO v2 product are much smaller than those observed by satellite and MAX-DOAS. However, the model data show a similar seasonality to the observational data. The significant underestimation of the TM4 NO_2 VCDs could be due to many factors, most importantly the limited spatial resolution of the model, which is especially relevant for species with strong horizontal gradients such as NO_2 and SO_2 (see Fig. 1). But possible errors in the emissions, transport schemes and/or chemical mechanisms might also play a role. The determination of the specific contributions of the different error sources should be the subject of future studies.
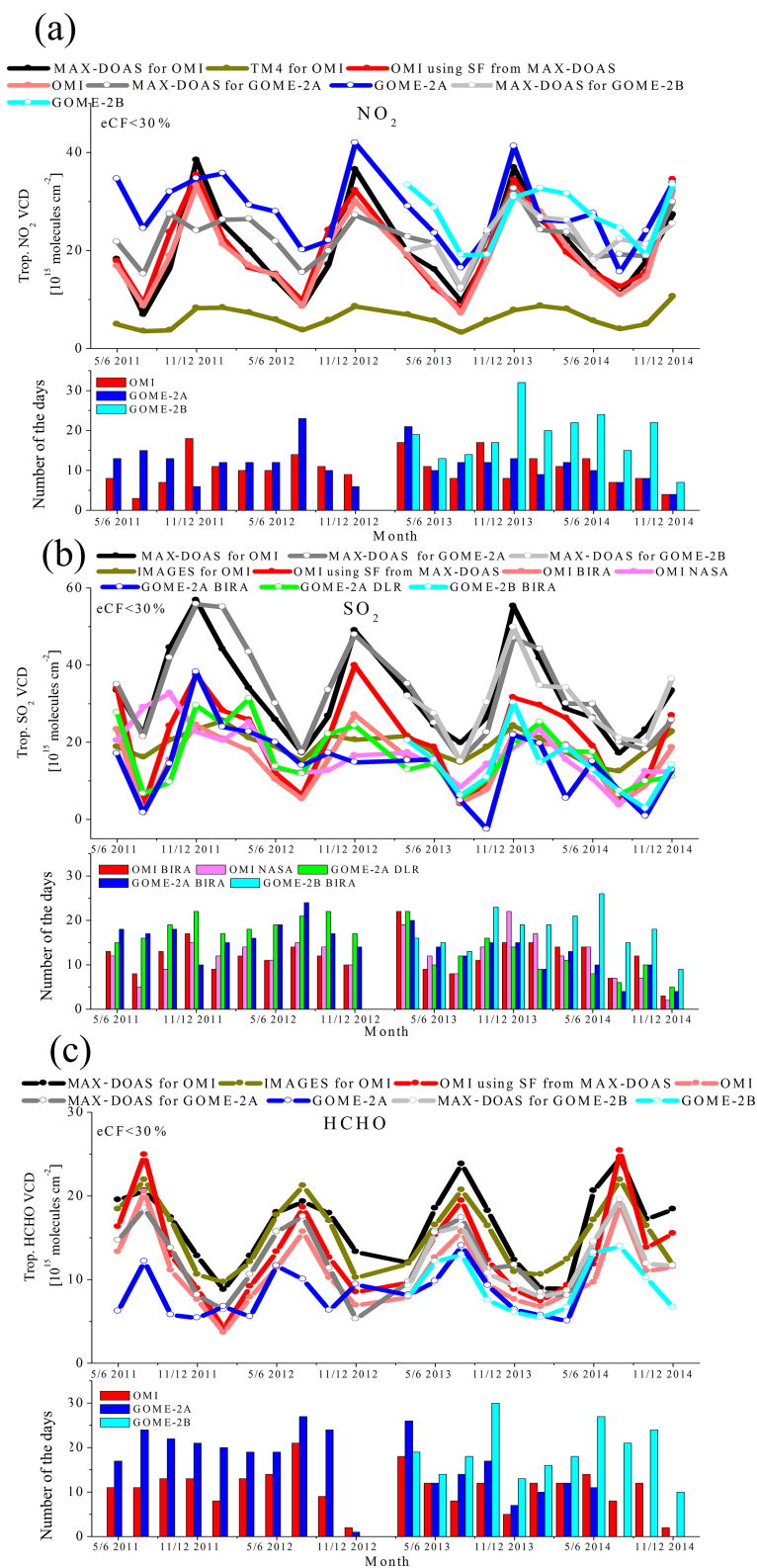
Figure 12. Bi-monthly-averaged tropospheric VCDs of NO$_2$ **(a)**, SO$_2$ **(b)** and HCHO **(c)** derived from coincident satellite and MAX-DOAS observations for eCF < 30 %. Also shown are the corresponding CTM results (TM4 for NO$_2$, IMAGES for SO$_2$ and HCHO). In all subfigures the red and light red lines indicate the improved OMI tropospheric VCDs using the SFs from MAX-DOAS and the VCDs from the original OMI products, respectively. The numbers of the available days are shown in the bottom panel of each subfigure.

3.3.2 SO$_2$

For SO$_2$, large differences between the absolute values of the satellite and MAX-DOAS results are found, but all data sets show a similar seasonality, with minima in summer and maxima in winter. The best agreement with MAX-DOAS results is found for the OMI BIRA VCD$_{SM}$, which displays an almost identical magnitude of the SO$_2$ annual variation (while still showing a large bias). Interestingly, a much better agreement is found for the modified OMI SO$_2$ than for the OMI BIRA using the SF from the CTM. However, the MAX-DOAS results are still significantly higher than the modified OMI products by about 1×10^{16} molecules cm^{-2} on average. Several reasons could contribute to the differences: (1) the horizontal gradient of SO$_2$ (see Fig. 1) and the MAX-DOAS pointing direction to the north can contribute to the differences of about 3×10^{15} molecules cm^{-2}. (2) The SO$_2$ cross section at 203 K is applied in the current version of the OMI BIRA product. It was found that the temperature dependence of the SO$_2$ cross sections (Bogumil et al., 2003) should also be considered using, for example, a post-correction method (BIRA-IASB, 2016). The correction can increase SO$_2$ VCDs by up to 1×10^{16} molecules cm^{-2}, with the highest absolute changes in winter. (3) The surface albedo used in the retrieval of the OMI BIRA product is taken from the climatological monthly minLER data from Kleipool et al. (2008) at 328 nm. We expect an uncertainty of the albedo of about 0.02. This will translate to an error of 15–20 % of the SO$_2$ VCDs. (4) Some unknown local emissions near the station might be underestimated by the satellite observations, but seen by the MAX-DOAS.

The BIRA GOME-2A/B and DLR GOME-2A data are consistent with each other, but show large differences to the corresponding MAX-DOAS results. The SO$_2$ VCDs simulated by IMAGES are systematically lower than the MAX-DOAS observations and show only a low amplitude of the seasonal variation. Same as for TM4 NO$_2$, the discrepancy of the IMAGES SO$_2$ VCDs needs a further investigation in future studies.

3.3.3 HCHO

Relatively good agreement between the satellite and MAX-DOAS observations of HCHO is found for all data sets (except GOME-2A before summer 2013). For OMI, a better agreement is found for the modified VCDs than for the original product, with a larger improvement in summer. GOME-2A/B products are consistent with each other but strongly underestimate the HCHO VCDs, especially in summer. It is interesting to note that the CTM results have a better consistency with the MAX-DOAS results than the OMI data. The much better consistency of the IMAGES HCHO VCDs compared to the SO$_2$ VCDs with MAX-DOAS measurements is also worth further investigation in the future. It should be noted that GOME-2A data before summer 2013 show the

Table 1. Mean ratios for the data presented in Fig. 13.

	Ratio$_{M-D}$ (G-2A / OMI)	Ratio$_{Sat}$ (G-2A / OMI)	Ratio$_{M-D}$ (G-2B / OMI)	Ratio$_{Sat}$ (G-2B / OMI)
NO$_2$	1.25	1.62	1.20	1.61
SO$_2$	1.02	1.02	1.01	1.09
HCHO	0.78	0.88	0.76	0.87

largest disagreement with the MAX-DOAS data. The reason for this phenomenon is not clear, but might be related to the different swath width in that period.

3.4 Diurnal variations characterized by combining the GOME-2A/B and OMI observations and the weekly cycle

Because of the morning and afternoon overpass time of GOME-2 and OMI, respectively, several studies (e.g. Boersma et al., 2008; Lin et al., 2010; De Smedt et al., 2015) investigated the differences of both data sets to characterize the diurnal variations of the TGs. The diurnal variations can be attributed to the complex interaction of the primary and secondary emission sources, depositions, atmospheric chemical reactions and transport processes. In this section we perform a similar study, but also include MAX-DOAS data coincident to the satellite observations. We calculate the ratios between the bi-monthly mean tropospheric VCDs from GOME-2A/B and OMI (Ratio$_{Sat}$) for each species and the corresponding ratios from the MAX-DOAS observations (Ratio$_{M-D}$). The results are shown in Fig. 13. The averaged Ratio$_{Sat}$ and Ratio$_{M-D}$ over the whole period are listed in Table 1. For NO$_2$, the Ratio$_{Sat}$ for both GOME-2 instruments show good agreement. Good agreement with the MAX-DOAS results is also found for the seasonal variation, but the absolute values differ. The systematic difference of Ratio$_{Sat}$ and Ratio$_{M-D}$ can be attributed to the known overestimation of the GOME-2 A/B tropospheric VCD compared to the MAX-DOAS results (see Fig. 12a). This finding also indicates that using GOME-2 and OMI data can lead to incorrect conclusions about the diurnal cycles of NO$_2$, as well as for the other TGs we investigated the ratios between the different data sets. However, because of the larger uncertainties compared to NO$_2$, the conclusions for SO$_2$ and HCHO should be treated with care. For SO$_2$, although Ratio$_{Sat}$ shows several deviations from Ratio$_{M-D}$, Ratio$_{M-D}$ and Ratio$_{Sat}$ are consistent on average and close to unity during a whole year indicating similar SO$_2$ VCDs around the overpass times of GOME-2 and OMI. For HCHO, on average good agreement between Ratio$_{Sat}$ and Ratio$_{M-D}$ is found for GOME-2A and GOME-2B (except some outliers of Ratio$_{Sat}$). Interestingly, both Ratio$_{Sat}$ and Ratio$_{M-D}$ are below unity, indicating lower HCHO VCDs in the morning than in the afternoon.

We evaluate the weekly cycles of the VCDs of the TGs observed by satellite instruments and the corresponding MAX-DOAS. The weekly cycles are shown in Fig. S17. In general,
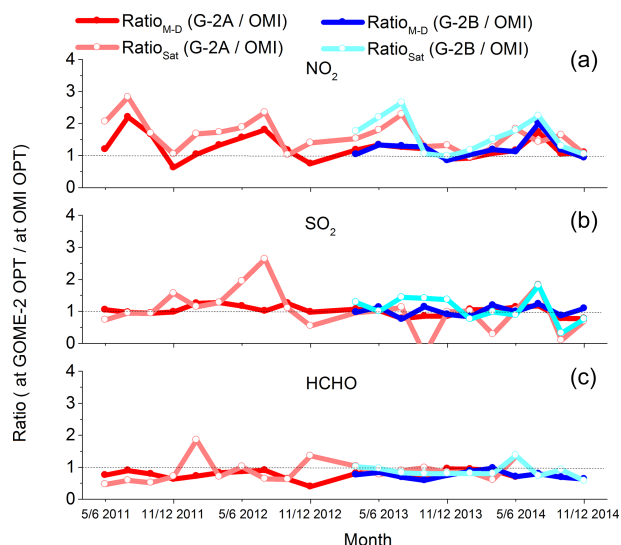
Figure 13. Ratios between the bi-monthly mean tropospheric VCDs from GOME-2A/B and OMI (Ratio$_{Sat}$), as well as the ratios between the corresponding MAX-DOAS observations (Ratio$_{M-D}$) for NO$_2$ **(a)**, SO$_2$ **(b)** and HCHO **(c)**, respectively. The light red (dark red) and light blue (dark blue) curves are corresponding to GOME-2A and GOME-2B results (coincident MAX-DOAS results with GOME-2A and GOME-2B), respectively. Note that for SO$_2$ the OMI and GOME-2A data from BIRA are used for the ratio calculations. The mean ratios for the shown data sets are presented in Table 1.

only the two GOME-2 instruments and the corresponding MAX-DOAS measurements observed considerable weekly cycles for NO$_2$.

3.5 Aerosol effects on the satellite results

In this section the aerosol effects on the satellite products are investigated. The OMI products (for SO$_2$ the OMI BIRA product is used) are used for this study because of their better consistency with the MAX-DOAS results compared to the products of the other satellite instruments. In Fig. 14 the absolute (top) and relative (bottom) differences of the TG VCDs between OMI and MAX-DOAS observations for individual OMI pixels are plotted against the AODs at 360 nm derived from the MAX-DOAS observations (Wang et al., 2017). It needs to be noted that the OMI VCDs used in Fig. 14 are the modified values using the SFs derived from MAX-DOAS observations in order to isolate the aerosol effects. The left subfigures show the comparisons for the data with eCF < 10 %, for which a potential cloud contamination is minimized. However, the eCF filter cannot exclude all clouds, and thus observations with thin cirrus clouds or other clouds with small geometric cloud fraction might still be included in the comparison, Therefore CTP > 900 hPa is used to further exclude residual clouds from the comparisons. The comparisons for

the data with eCF < 10 % and CTP > 900 hPa are shown in the centre column of Fig. 14. Finally, observations with small TG VCDs (NO$_2$ < 2 × 10^{16} molecules cm^{-2}, SO$_2$ < 2 × 10^{16} molecules cm^{-2} and HCHO < 1 × 10^{16} molecules cm^{-2}) are also skipped to minimize the influence of non-polluted observations on the comparison. The results after applying all three filters are shown in the right part of Fig. 14.

A systematically increasing underestimation of the OMI VCDs compared to MAX-DOAS VCDs with increasing AOD can been seen for NO$_2$ and SO$_2$. This indicates the effects of aerosols on the satellite products. However, here one aspect needs to be considered. Besides aerosols, residual (low altitude) clouds might also still have an effect on the comparison results. In order to quantify their potential effect, we performed RTM simulations (for details see Sect. S3) to evaluate the difference of TG AMFs which are calculated for either aerosols or residual clouds. As residual clouds we chose either homogeneous optically thin clouds covering the whole satellite pixel or optically thick clouds covering only a small geometric fraction of the satellite pixel. For both types of clouds, the extinction profiles were chosen to match the radiance and O$_4$ SCDs at 477 nm of the aerosol cases. We found that the differences of the AMFs for aerosols and residual clouds are generally smaller than 10 % for NO$_2$, and 5 % for SO$_2$ and HCHO. It should be noted that the actual effect of residual clouds is in general much smaller, because usually aerosols and clouds are present at the same time. Thus we conclude that residual clouds have a negligible effect on the comparison results shown in Fig. 14.

The dependence on AOD shown in Fig. 14 is strongest for NO$_2$. Besides the larger uncertainties of the HCHO and SO$_2$ retrievals, this is probably mainly related to the fact that in contrast to the DOMINO NO$_2$ product, for the OMI BIRA SO$_2$ and HCHO products no cloud correction is performed, i.e. a clear-sky AMF (for a Rayleigh scattering atmosphere) is applied in cases of eCF < 10 %.

Aerosols affect the satellite TG retrievals in two ways: first they affect the cloud retrievals of eCF and CTP and thus the TG AMFs if a cloud correction is applied in the satellite retrievals. If a Lambertian cloud model is used, the effect of this implicit aerosol correction depends systematically on the aerosol properties (Boersma et al., 2011; Lin et al., 2014; Wang et al., 2015; Chimot et al., 2016). For mostly scattering aerosols at high altitudes, the implicit aerosol correction can largely account for the aerosol effect on the TG products (Boersma et al., 2011). However, in some important cases (for low altitude aerosols with high AOD and small SSA) the implicit correction might even increase the errors of the AMF Castellanos et al. (2015).

Besides the aerosol effect on the cloud retrievals and cloud correction schemes, aerosols also directly affect the AMF compared to AMFs for pure Rayleigh scattering conditions. Leitão et al. (2010) and Chimot et al. (2016) found that the influence of aerosols on the satellite retrievals mainly de-
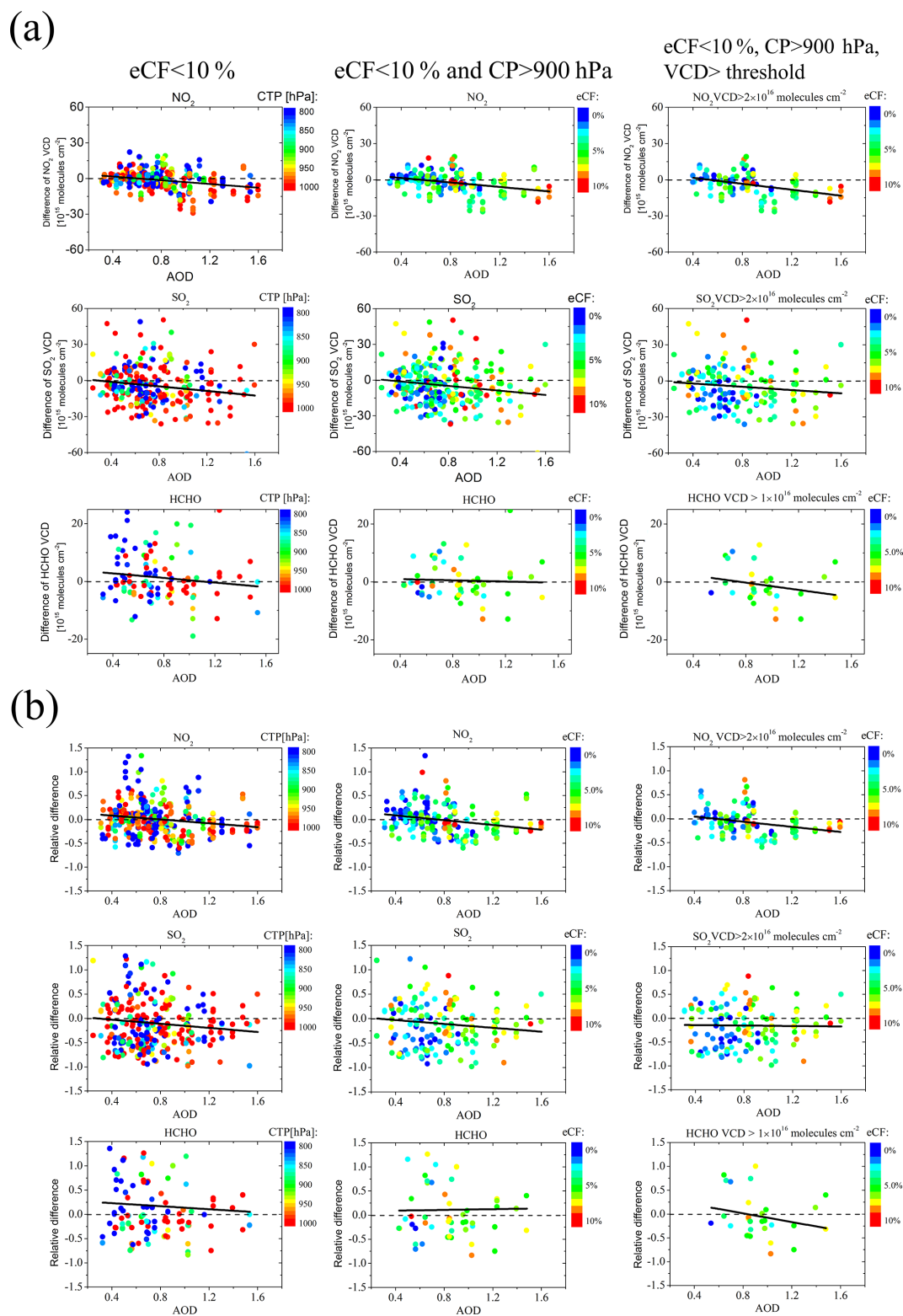
Figure 14. Absolute differences **(a)** and relative differences **(b)** of tropospheric VCDs of NO$_2$, SO$_2$ and HCHO between individual OMI observations and MAX-DOAS observations plotted against the AODs derived from the MAX-DOAS observations. The data are differently screened in the left, centre and right panels: eCF < 10 % for the left; eCF < 10 % and CTP > 900 hPa for the centre; and eCF < 10 %, CTP > 900 hPa, and VCD > a specific threshold for the right (see text). Note that the OMI VCDs are the modified values using SFs derived from MAX-DOAS observations.

pends on the relative vertical distributions of aerosols and TGs. To further quantify both aerosol effects on the satellite retrievals, we performed RTM simulations for typical scenarios of aerosols and TGs in Wuxi.

In Fig. 15 the OMI eCF and CTP (for eCF < 10 % and CTP > 900 hPa) are plotted against the AOD at 360 nm derived from MAX-DOAS observation (similar plots for the AOD at 340 nm derived from the nearby Taihu AERONET station (Holben et al., 1998, 2001) are shown in Fig. S18). The results indicate a systematic increase of eCF and CTP with increasing AOD, but also a large scatter, especially for AOD < 1. The systematic increase of eCF and CTP with AOD is consistent with the model simulations in Chimot et al. (2016). The variability of eCF and CTP can be attributed to different observation geometries as well as uncertainties of the cloud retrievals (e.g. related to measurement uncertainties and/or the variability of surface properties). The frequency distributions of eCF and CTP are also shown in Fig. 15. Considering this frequency distribution and the variability of eCF and CTP, eCF of 5 and 10 % as well as CTP of 900 and 1000 hPa are used in the following for the RTM simulations to estimate the errors caused by aerosols. As aerosol properties we chose AOD values of 0.8 and 1.5, which represent typical and high aerosol loads at Wuxi, respectively. As vertical profile we chose an average profile derived from MAX-DOAS measurements under clear-sky conditions (Wang et al., 2017), which is shown in Fig. S19. The aerosol optical properties (single scattering albedo of 0.9 at 438 nm, asymmetry parameter of 0.72 at 438 nm, and Ångström parameter of 0.85 at the wavelength pair of 340 and 440 nm) are taken from the AERONET observations at the nearby Taihu station (Holben et al., 1998, 2001). We use either SFs derived from the Wuxi MAX-DOAS observations or from the CTM simulations, which are also used for the satellite retrievals. The SFs of the TGs are shown in Fig. S19. The surface albedo is set to 0.1 for NO$_2$ and 0.05 for SO$_2$ and HCHO simulations, based on the averaged value of the surface reflectivity data base derived from OMI by Kleipool et al. (2008) over Wuxi station. Temperature and pressure profiles are derived from the US standard atmosphere data base. The RTM simulations are performed for five typical satellite observation geometries shown in Table 2. The TG BAMFs and AMFs were simulated for NO$_2$ at 435 nm, HCHO at 337 nm and SO$_2$ at 319 nm using the RTM McArtim 3 (Deutschmann et al., 2011). Since the wavelength range covered by the AERONET measurements does not extend to the ultraviolet range, the same aerosol properties derived from the AERONET observations are used for the simulations at 319 nm (SO$_2$) and 337 nm (HCHO) and those at 435 nm (NO$_2$).

The simulations are performed for four scenarios: (1) pure Rayleigh scattering conditions (BAMF$_{clear-sky}$ and AMF$_{clear-sky}$); (2) aerosol profiles with the AOD of 0.8 and 1.5 (BAMF$_{explicit}$ and AMF$_{explicit}$); (3) Lambertian clouds at the surface (CTP of about 1000 hPa) with an eCF of 10 and

Table 2. Observation geometry scenarios for BAMF and AMF calculations with different aerosol and cloud assumptions.

Scenario	Solar zenith angle [°]	View zenith angle [°]	Relative azimuth angle [°]
g1	40	30	180
g2	10	30	180
g3	70	30	180
g4	40	0	180
g5	40	30	0

5 % (BAMF$_{low-cloud}$ and AMF$_{low-cloud}$); and (4) Lambertian clouds at 1 km (CTP of about 900 hPa) with an eCF of 10 and 5 % (BAMF$_{high-cloud}$ and AMF$_{high-cloud}$). The cases 3 and 4 represent the implicit aerosol correction. Note that we use the same cloud model (Lambertian reflector with an albedo of 0.8) as in the official OMI cloud and TG retrievals.

The BAMFs for the different TGs simulated for the four scenarios at the g1 observation geometry (40° SZA, 180° RAA and 30° VZA) are shown in Fig. 16a. Note that the results of scenario 3 and 4 with eCF of 10 % are shown. The relative differences of the BAMFs for clear sky and clouds compared to those explicitly considering aerosols (AOD of either 0.8 or 1.5) are shown in Fig. 16b and c, respectively. For all TGs, the clear-sky BAMFs are higher close to the surface and lower for higher altitudes than the explicit aerosol BAMFs, which is caused by the additional aerosol scattering. The BAMFs near the surface for the cloud scenarios are either larger ("low cloud scenario") or smaller ("high cloud scenario") than the aerosol AMFs. For both cloud scenarios the BAMFs are higher than the aerosol BAMFs at higher altitudes. Overall the differences of the BAMFs for the cloud scenarios compared to the aerosol BAMFs are larger than the differences between the clear-sky BAMFs and aerosol BAMFs. For the higher AOD (1.5) in general larger differences are found than for the small AOD (0.8).

The AMFs of NO$_2$, SO$_2$ and HCHO for the four scenarios are calculated using the corresponding BAMFs and typical SFs (shown in Fig. S19) derived from MAX-DOAS measurements and CTM simulations by Eq. (2). The relative differences of the AMFs for clear sky and for two cloud scenarios compared to the AMFs for the explicit aerosol simulations for five different satellite observation geometries (listed in Table 2) are shown in Fig. 17. Figure 17a and b show the results for AOD of 0.8 and 1.5, respectively. It can be seen that the implicit aerosol correction can lead to large deviations, especially for the "low cloud scenario". The deviation for the "high cloud scenario" is close to the deviation of clear-sky AMF, and even smaller in some cases, due to the compensation of the partial AMF below and above the cloud plane. Here it should be noted that for aerosol layers reaching to higher altitudes the errors of the high cloud scenario will in general increase. For the "low cloud scenario" the devi-
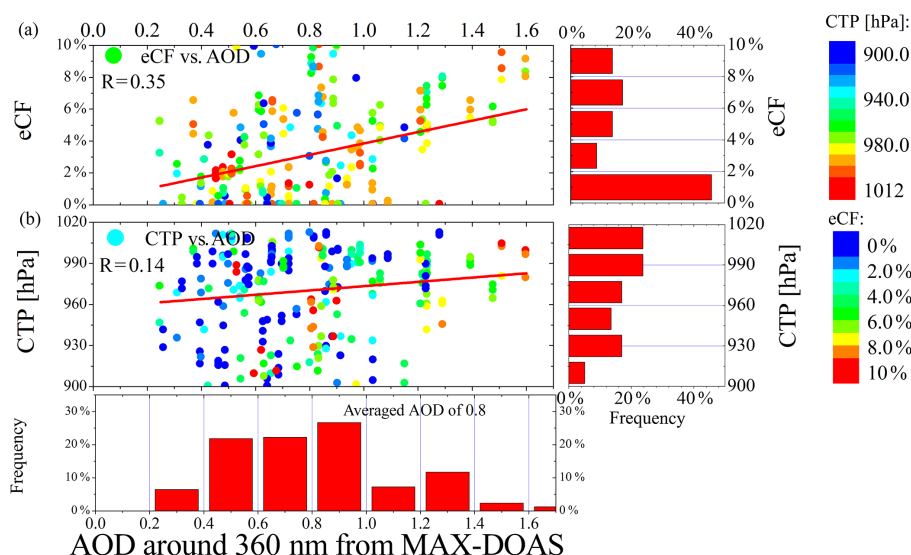
Figure 15. eCF and CTP from the OMI cloud algorithm for individual OMI observations are plotted against AOD at 360 nm derived from MAX-DOAS observation (for eCF < 10 % and CTP > 900 hPa). The red bars on the right and bottom indicate the frequency of eCF, CTP and AOD in different value intervals. The red lines are the linear regressions of the scatter plots. The correlation coefficients are shown in the figure. The colour of the dots in **(a)** and **(b)** indicates CTP and eCF, respectively.

ation increases with increasing eCF. As already seen for the BAMFs, the deviations of the clear-sky AMFs and Lambertian cloud AMFs also increase with AOD. Overall the biases introduced by the implicit aerosol correction (3 to 85 % for NO_2, −4 to 26 % for HCHO and −2 to 45 % for SO_2) are significantly larger than those for the clear-sky AMFs (5 to 50 % for NO_2, −12 to −5 % for HCHO and −9 to 1 % for SO_2). One important finding is that the stronger overestimation of the NO_2 AMF for the "high cloud scenario" than for the "low cloud scenario", as well as for eCF of 10 % than 5 %, can explain well the observed dependence of the magnitude of the underestimation of the OMI NO_2 VCD on the CTP and eCF, as shown in Fig. 14. Therefore we conclude that for measurements at Wuxi with strong aerosol loads, the implicit aerosol correction in general leads to larger biases of the derived TG VCDs than the use of a clear-sky AMF.

4 Conclusions

Tropospheric VCDs of NO_2, SO_2 and HCHO derived from OMI, GOME-2A/B observations are validated using MAX-DOAS measurements in Wuxi, China, from May 2011 to December 2014. Tropospheric VCDs and vertical profiles of aerosols and TGs derived from the Wuxi MAX-DOAS observations using the PriAM OE-based algorithm are applied in this validation study.

We compare the daily-averaged tropospheric VCDs from the satellite products with the corresponding MAX-DOAS results under clear-sky conditions (eCF < 10 %). For NO_2, good agreement (R^2 of 0.73 and systematic bias of 1 %) is found for the DOMINO v2 product. For both GOME-2 products (TM4NO2A), much weaker correlation (R^2 of 0.33 for GOME-2A and 0.2 for GOME-2B) is found with a similar systematic bias of about 30 %. For SO_2, the OMI BIRA product shows a much better correlation (R^2 of 0.47) than the OMI NASA product (R^2 =0.12), the GOME-2A BIRA product (R^2 = 0.07), the GOME-2A DLR product (R^2 = 0.09) and the GOME-2B BIRA product (R^2 = 0.28). All of these products systematically underestimate the SO_2 tropospheric VCDs by about 40 to 60 %. For HCHO, the best agreement is found for the GOME-2B product with R^2 of 0.53 and a systematic bias of −12 %. The OMI and GOME-2A products have lower R^2 of 0.17 and 0.18, respectively, with a similar systematic bias of about −20 %.

In general, we expect that the VCDs from MAX-DOAS observations have much lower uncertainties than those from satellite observations. However, we should also consider the total uncertainties of the MAX-DOAS VCDs of NO_2, SO_2 and HCHO of about 25, 31 and 54 %, respectively (Wang et al., 2017). Moreover, MAX-DOAS has low sensitivity to high altitudes, above about 1–2 km. This can cause an underestimation of the VCDs retrieved from MAX-DOAS. The strength of this effect depends on the vertical distribution of the species, the atmospheric visibility and the observation geometry of the MAX-DOAS measurement. In this study we do not discuss these issues in more detail. This should be done in further studies. Nevertheless, the sensitivity of MAX-DOAS observations to the boundary layer is much larger than for satellite observations, and this is the altitude range in which the pollutants are usually accumulated. Thus it is reasonable to assume that the systematic differences between both data
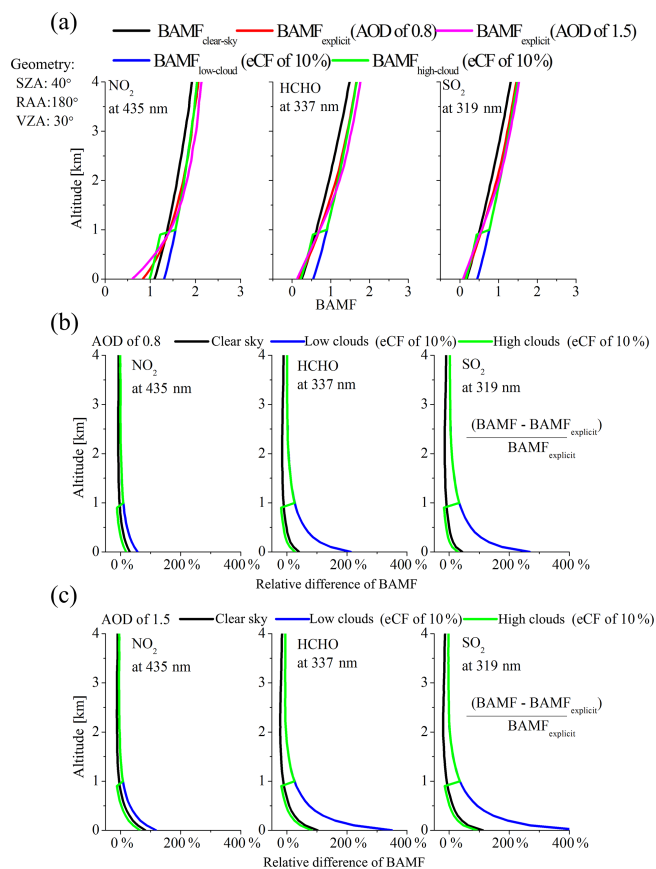
Figure 16. (a) Simulated BAMF$_{clear-sky}$, BAMF$_{explicit}$ for AOD of 0.8 and 1.5, BAMF$_{low-cloud}$ (cloud at surface) and BAMF$_{high-cloud}$ (cloud at 1 km) of NO$_2$ at 435 nm, HCHO at 337 nm and SO$_2$ at 319 nm for one typical satellite observation (SZA of 40°, RAA of 180° and VZA of 30°). An effective cloud fraction of 10 % is used in the calculations. **(b)** Relative differences of BAMF$_{clear-sky}$, BAMF$_{low clouds}$ and BAMF$_{high-clouds}$ compared to BAMF$_{explicit}$ for AOD of 0.8. **(c)** Same as **(b)** but BAMF$_{explicit}$ for AOD of 1.5.

Figure 17. Relative differences between AMFs calculated for different cloud assumptions (for detail see text) and AMFs for explicit aerosol profiles for three TGs. The labels at the x axis indicate five different observation geometries (see Table 2). The MAX-DOAS and CTM SFs are used for the calculations shown in the left and right column. Explicit aerosol profiles of AOD of 0.8 and 1.5 are used in **(a)** and **(b)**, respectively.

sets are mainly attributed to the errors of the satellite observations.

We investigated the effects of clouds on the MAX-DOAS results and satellite products and find that the consistency (correlations and systematic bias) of satellite data with MAX-DOAS results deteriorates with increasing eCF. The cloud effects become significant for eCF > 40 % for the OMI DOMINO NO$_2$ product, > 30 % for the GOME-2A/B NO$_2$ products, > 10 % for the OMI BIRA SO$_2$ product, > 20 % for the OMI NASA SO$_2$ product, > 30 % for the GOME-2A/B BIRA SO$_2$ products and > 30 % for all HCHO products. Here it should be noted that, except for optically thick clouds and fog, the cloud effects on the MAX-DOAS results are negligible. It should also be noted that these findings are obtained for the original satellite products, namely using SF from CTM or assumed fixed SF. In addition, the different
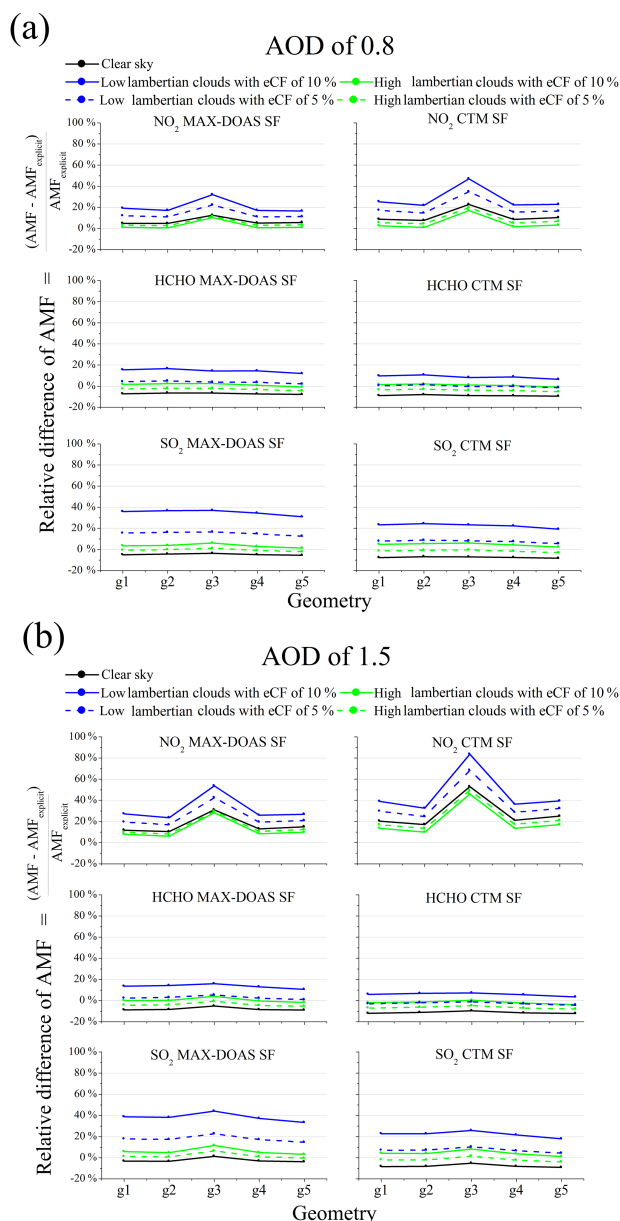
thresholds of eCF could also be related to the properties of the different cloud products. This effect is not discussed in this paper, and further studies on this would be valuable. In general, it should be noted that these results are representative for conditions like in Wuxi, and might be different for other locations.

In the OMI DOMINO NO_2, OMI BIRA SO_2 and HCHO products, the a priori SFs of the TGs are obtained from CTM. We compare these SFs (derived from TM4 for NO_2, and IMAGES for SO_2 and HCHO) with those derived from MAX-DOAS observation and find substantial differences. We investigate the effect of using the MAX-DOAS SFs in the satellite retrievals. Under clear-sky conditions, the application of the SFs from MAX-DOAS changes the SO_2 and HCHO AMFs by about 18 and 11 %, respectively, but has almost no impact on the NO_2 AMFs. We find that the modified satellite VCDs based on the MAX-DOAS SF show much better agreement with the MAX-DOAS results (considerably higher correlation coefficients R^2 and smaller systematic biases) than the original satellite data. The improvement is strongest for periods with large TG VCDs, namely for NO_2 and SO_2 in winter and for HCHO in summer. In these periods, NO_2, SO_2 and HCHO VCD change by up to 10, 47 and 35 %, respectively. We also found that the effect of using the MAX-DOAS SFs in the satellite retrievals increases for increasing eCF. This finding is mainly caused by the partial satellite AMF above 4 km and the significant reduction of the partial satellite AMF below 4 km in cloudy situations. In addition, the low sensitivity of MAX-DOAS above about 1–2 km could cause an underestimation of the MAX-DOAS SFs of the TGs at higher altitudes, especially for SO_2 and HCHO. This effect could cause the underestimation of the AMFs and an overestimation of the VCDs by using the MAX-DOAS SFs.

We also compare the bi-monthly mean satellite products to the corresponding MAX-DOAS results. The relative seasonal variations of the NO_2, SO_2 and HCHO tropospheric VCDs from the different satellite products agree well with the corresponding MAX-DOAS results. The best consistency is found for the OMI DOMINO NO_2 product. A systematic overestimation of the NO_2 VCDs is found for GOME-2A/B NO_2 products. All SO_2 satellite products show similar SO_2 VCDs and a systematic underestimation of about 2×10^{16} molecules cm^{-2}. Based on the studies on the OMI BIRA product, the systematic underestimation could be attributed to a combined effect of errors of the SFs, horizontal gradients of the SO_2 distribution, the temperature dependence of the SO_2 cross section, and uncertainties of the surface albedo and local emissions. The OMI NASA, GOME-2A BIRA and DLR SO_2 products show a larger random variability than the OMI and GOME-2B BIRA SO_2 products. All OMI and GOME-2A/B products systematically underestimate the tropospheric HCHO VCDs by about 5×10^{15} molecules cm^{-2}, while showing a similar seasonality to the MAX-DOAS results. The biases found for the bi-monthly-averaged satellite TG VCDs are consistent with those found for the daily comparisons.

We compared the diurnal variations (ratios of morning and afternoon values) of TGs by combining GOME-2A/B (morning overpass) with OMI (afternoon overpass) observations with the corresponding MAX-DOAS observations. Gener-

ally higher NO_2 values and lower HCHO values in the morning are acquired, but no significant diurnal cycle was found for SO_2. Consistent diurnal variations of HCHO and SO_2 between satellite and MAX-DOAS observations were derived. The combined satellite observations systematically overestimate the magnitude of the NO_2 diurnal variation compared to MAX-DOAS due to the overestimation of the NO_2 VCDs by GOME-2. In addition no significant weekly cycle was found for the three TGs in the satellite and MAX-DOAS data.

Finally we studied the effects of aerosols on the OMI products over the Wuxi station based on the MAX-DOAS observations. We find that the underestimation of the TG VCDs, derived from satellite observations for mainly cloud-free observations compared to the MAX-DOAS observations, systematically increases with AOD. We also investigate the aerosol effect based on RTM simulations. Here, in particular, it is possible to separate the aerosol effect into two contributions: (a) the effect of using a clear-sky AMF instead of an AMF explicitly taking into account the aerosol effects, and (b) the effect of aerosols on the cloud retrievals, which are used in the satellite TG retrievals (implicit aerosol correction). We find that for the measurements affected by high aerosol loads in Wuxi, in general the effect of the implicit cloud correction on the retrieved TG VCDs is much stronger than the difference of a clear-sky AMF compared to an AMF explicitly taking into account the aerosol extinction. We also showed that for eCF < 10 % and CTP > 900 hPa, the effect of residual clouds can be neglected if aerosol extinction is explicitly taken into account. Moreover, the observed underestimation of the OMI NO_2 VCD for large AOD can be explained well by the error caused by the implicit aerosol correction. Therefore it might be reasonable to apply clear-sky AMFs in the satellite retrievals of tropospheric TG VCDs in cases of low cloud altitudes (CTP > 900 hPa) and low cloud fractions (eCF < 10 %) if explicit aerosol information is not available.

The Supplement related to this article is available online at doi:10.5194/acp-17-5007-2017-supplement.

References

Acarreta, J. R., De Haan, J. F., and Stammes, P.: Cloud pressure retrieval using the O$_2$–O$_2$ absorption band at 477 nm, J. Geophys. Res.-Atmos., 109, D05204, doi:10.1029/2003JD003915, 2004.

Barkley, M. P., Kurosu, T. P., Chance, K., De Smedt, I., Van Roozendael, M., Arneth, A., Hagberg, D., and Guenther, A.: Assessing sources of uncertainty in formaldehyde air mass factors over tropical South America: Implications for top-down isoprene emission estimates, J. Geophys. Res.-Atmos., 117, D13304, doi:10.1029/2011JD016827, 2012.

Bauwens, M., Stavrakou, T., Müller, J.-F., De Smedt, I., Van Roozendael, M., van der Werf, G. R., Wiedinmyer, C., Kaiser, J. W., Sindelarova, K., and Guenther, A.: Nine years of global hydrocarbon emissions based on source inversion of OMI formaldehyde observations, Atmos. Chem. Phys., 16, 10133–10158, doi:10.5194/acp-16-10133-2016, 2016.

Beirle, S. and Wagner, T.: Tropospheric vertical column densities of NO$_2$ from SCIAMACHY, available at: http://projects.knmi.nl/sciamachy/products/NO2/NO2tc_v1_0_MPI_AD.pdf (last access: 5 April 2017), 2010.

Beirle, S., Platt, U., Wenig, M., and Wagner, T.: Weekly cycle of NO$_2$ by GOME measurements: a signature of anthropogenic sources, Atmos. Chem. Phys., 3, 2225–2232, doi:10.5194/acp-3-2225-2003, 2003.

Beirle, S., Boersma, K. F., Platt, U., Lawrence, M. G., and Wagner, T.: Megacity emissions and lifetimes of nitrogen oxides probed from space, Science, 333, 1737–1739, 2011.

BIRA-IASB: S5P/TROPOMI SO2 ATBD, Issue 1.0.0, available at: http://www.tropomi.eu/sites/default/files/files/S5P-BIRA-L2-ATBD-SO2_400E_TROPOMI_v1p0p0_20160205.pdf, (last access: 26 July 2014), 2016.

Bobrowski, N., Honninger, G., Galle, B., and Platt, U.: Detection of bromine monoxide in a volcanic plume, Nature, 423, 273–276, 2003.

Boersma, K. F., Eskes, H. J., and Brinksma, E. J.: Error Analysis for Tropospheric NO$_2$ Retrieval from Space, J. Geophys. Res., 109, D04311, doi:10.1029/2003JD003962, 2004.

Boersma, K. F., Eskes, H. J., Veefkind, J. P., Brinksma, E. J., van der A, R. J., Sneep, M., van den Oord, G. H. J., Levelt, P. F.,

Stammes, P., Gleason, J. F., and Bucsela, E. J.: Near-real time retrieval of tropospheric NO$_2$ from OMI, Atmos. Chem. Phys., 7, 2103–2118, doi:10.5194/acp-7-2103-2007, 2007.

Boersma, K. F., Jacob, D. J., Eskes, H. J., Pinder, R. W., and Wang, J.: Intercomparison of SCIAMACHY and OMI tropospheric NO$_2$ columns: Observing the diurnal evolution of chemistry and emissions from space, J. Geophys. Res., 113, D16S26, doi:10.1029/2007JD008816, 2008.

Boersma, K. F., Eskes, H. J., Dirksen, R. J., van der A, R. J., Veefkind, J. P., Stammes, P., Huijnen, V., Kleipool, Q. L., Sneep, M., Claas, J., Leitão, J., Richter, A., Zhou, Y., and Brunner, D.: An improved tropospheric NO$_2$ column retrieval algorithm for the Ozone Monitoring Instrument, Atmos. Meas. Tech., 4, 1905–1928, doi:10.5194/amt-4-1905-2011, 2011.

Bogumil, K., Orphal, J., Homann, T., Voigt, S., Spietz, P., Fleischmann, O. C., Vogel, A., Hartmann, M., Kromminga, H., Bovensmann, H., Frerick, J., and Burrows, J. P.: Measurements of molecular absorption spectra with the SCIAMACHY pre-flight model: instrument characterization and reference data for atmospheric remote-sensing in the 230–2380 nm region, J. Photoch. Photobio. A, 157, 167–184, 2003.

Bovensmann, H., Burrows, J. P., Buchwitz, M., Frerick, J., Noël, S., Rozanov, V. V., Chance, K. V., and Goede, A. P. H.: SCIAMACHY: Mission objectives and measurement modes, J. Atmos. Sci., 56, 127–150, 1999.

Brinksma, E. J., Pinardi, G., Volten, H., Braak, R., Richter, A., Schönhardt, A., van Roozendael, M., Fayt, C., Hermans, C., Dirksen, R. J., Vlemmix, T., Berkhout, A. J. C., Swart, D. P. J., Oetjen, H., Wittrock, F., Wagner, T., Ibrahim, O. W., de Leeuw, G., Moerman, M., Curier, R. L., Celarier, E. A., Cede, A., Knap, W. H., Veefkind, J. P., Eskes, H. J., Allaart, M., Rothe, R., Piters, A. J. M., and Levelt, P. F.: The 2005 and 2006 DANDELIONS NO$_2$ and aerosol intercomparison campaigns, J. Geophys. Res., 113, D16S46, doi:10.1029/2007JD008808, 2008.

Burrows, J. P., Weber, M., Buchwitz, M., Rozanov, V., Ladstätter-Weißenmayer, A., Richter, A., DeBeek, R., Hoogen, R., Bramstedt, K., Eichmann, K. U., and Eisinger, M.: The global ozone monitoring experiment (GOME): Mission concept and first scientific results, J. Atmos. Sci., 56, 151–175, 1999.

Cahalan, R. F., Ridgway, W., Wiscombe, W. J., Gollmer, S., and Harshvardhan: Independent pixel and Monte Carlo estimates of stratocumulus albedo, J. Atmos. Sci., 51 , 3776–3790, 1994.

Callies, J., Corpaccioli, E., Eisinger, M., Hahne, A., and Lefebvre, A.: GOME-2 – MetOp's Second Generation Sensor for Operational Ozone Monitoring, ESA Bulletin, 102, 28–36, 2000.

Carn, S. A., Krueger, A. J., Krotkov, N. A., and Gray, M. A.: Fire at Iraqi sulfur plant emits SO$_2$ clouds detected by Earth Probe TOMS, Geophys. Res. Lett., 31, L19105, doi:10.1029/2004GL020719, 2004.

Castellanos, P., Boersma, K. F., Torres, O., and de Haan, J. F.: OMI tropospheric NO$_2$ air mass factors over South America: effects of biomass burning aerosols, Atmos. Meas. Tech., 8, 3831–3849, doi:10.5194/amt-8-3831-2015, 2015.

Chan, K. L., Hartl, A., Lam, Y. F., Xie, P. H., Liu, W. Q., Cheung, H. M., Lampel, J., Pöhler, D., Li, A., Xu, J., Zhou, H. J., Ning, Z., and Wenig, M. O.: Observations of tropospheric NO$_2$ using ground based MAX-DOAS and OMI measurements during the Shanghai World Expo 2010, Atmos. Environ., 119, 45–58, 2015.

Chance, K., Palmer, P. I., Spurr, R. J., Martin, R. V., Kurosu, T. P., and Jacob, D. J.: Satellite observations of formaldehyde over North America from GOME, Geophys. Res. Lett., 27, 3461–3464, 2000.

Chen, D., Zhou, B., Beirle, S., Chen, L. M., and Wagner, T.: Tropospheric NO$_2$ column densities deduced from zenith-sky DOAS measurements in Shanghai, China, and their application to satellite validation, Atmos. Chem. Phys., 9, 3641–3662, doi:10.5194/acp-9-3641-2009, 2009.

Chimot, J., Vlemmix, T., Veefkind, J. P., de Haan, J. F., and Levelt, P. F.: Impact of aerosols on the OMI tropospheric NO$_2$ retrievals over industrialized regions: how accurate is the aerosol correction of cloud-free scenes via a simple cloud model?, Atmos. Meas. Tech., 9, 359–382, doi:10.5194/amt-9-359-2016, 2016.

Clémer, K., Van Roozendael, M., Fayt, C., Hendrick, F., Hermans, C., Pinardi, G., Spurr, R., Wang, P., and De Mazière, M.: Multiple wavelength retrieval of tropospheric aerosol optical properties from MAXDOAS measurements in Beijing, Atmos. Meas. Tech., 3, 863–878, doi:10.5194/amt-3-863-2010, 2010.

Crippa, M., Ciarelli, G., Piazzalunga, A., Schwikowski, M., Abbaszade, G., Schnelle-Kreis, J., Zimmermann, R., An, Z., Szidat, S., Baltensperger, U., El Haddad, I., and Prevot, A. S.: High secondary aerosol contribution to particulate pollution during haze events in China, Nature, 514, 218–222, 2014.

De Smedt, I., Müller, J.-F., Stavrakou, T., van der A, R., Eskes, H., and Van Roozendael, M.: Twelve years of global observations of formaldehyde in the troposphere using GOME and SCIAMACHY sensors, Atmos. Chem. Phys., 8, 4947–4963, doi:10.5194/acp-8-4947-2008, 2008.

De Smedt, I., Van Roozendael, M., Stavrakou, T., Müller, J.-F., Lerot, C., Theys, N., Valks, P., Hao, N., and van der A, R.: Improved retrieval of global tropospheric formaldehyde columns from GOME-2/MetOp-A addressing noise reduction and instrumental degradation issues, Atmos. Meas. Tech., 5, 2933–2949, doi:10.5194/amt-5-2933-2012, 2012.

De Smedt, I., Stavrakou, T., Hendrick, F., Danckaert, T., Vlemmix, T., Pinardi, G., Theys, N., Lerot, C., Gielen, C., Vigouroux, C., Hermans, C., Fayt, C., Veefkind, P., Müller, J.-F., and Van Roozendael, M.: Diurnal, seasonal and long-term variations of global formaldehyde columns inferred from combined OMI and GOME-2 observations, Atmos. Chem. Phys., 15, 12519–12545, doi:10.5194/acp-15-12519-2015, 2015.

Deutschmann, T., Beirle, S., Frieß, U., Grzegorski, M., Kern, C., Kritten, L., Platt, U., Prados-Román, C., Puĩ, J., Wagner, T., and Werner, B.: The Monte Carlo atmospheric radiative transfer model McArtim: Introduction and validation of Jacobians and 3D features, J. Quant. Spectrosc. Ra., 112, 1119–1137, 2011.

Ding, J., van der A, R. J., Mijling, B., Levelt, P. F., and Hao, N.: NO$_x$ emission estimates during the 2014 Youth Olympic Games in Nanjing, Atmos. Chem. Phys., 15, 9399–9412, doi:10.5194/acp-15-9399-2015, 2015.

Dirksen, R. J., Boersma, K. F., Eskes, H. J., Ionov, D. V., Bucsela, E. J., Levelt, P. F., and Kelder, H. M.: Evaluation of stratospheric NO$_2$ retrieved from the Ozone Monitoring Instrument: intercomparison, diurnal cycle and trending, J. Geophys. Res., 116, D08305, doi:10.1029/2010JD014943, 2011.

Eisinger, M. and Burrows, J. P.: Tropospheric sulfur dioxide observed by the ERS-2 GOME instrument, Geophys. Res. Lett., 25, 4177–4180, 1998.

Environmental Protection Agency: National air quality and emissions trends report 1998, Rep. EPA 454/R-00-003, 1998.

Eskes, H. J. and Boersma, K. F.: Averaging kernels for DOAS total-column satellite retrievals, Atmos. Chem. Phys., 3, 1285–1291, doi:10.5194/acp-3-1285-2003, 2003.

Frieß, U., Monks, P. S., Remedios, J. J., Rozanov, A., Sinreich, R., Wagner, T., and Platt, U.: MAX-DOAS O$_4$ measurements: A new technique to derive information on atmospheric aerosols: 2. Modeling studies, J. Geophys. Res., 111, D14203, doi:10.1029/2005JD006618, 2006.

Frieß, U., Sihler, H., and Sander, R.: The vertical distribution of BrO and aerosols in the Arctic: Measurements by active and passive differential optical absorption spectroscopy, J. Geophys. Res., 116, D00R04, doi:10.1029/2011JD015938, 2011.

Frieß, U., Klein Baltink, H., Beirle, S., Clémer, K., Hendrick, F., Henzing, B., Irie, H., de Leeuw, G., Li, A., Moerman, M. M., van Roozendael, M., Shaiganfar, R., Wagner, T., Wang, Y., Xie, P., Yilmaz, S., and Zieger, P.: Intercomparison of aerosol extinction profiles retrieved from MAX-DOAS measurements, Atmos. Meas. Tech., 9, 3205–3222, doi:10.5194/amt-9-3205-2016, 2016.

Fu, G. Q., Xu, W. Y., Yang, R. F., Li, J. B., and Zhao, C. S.: The distribution and trends of fog and haze in the North China Plain over the past 30 years, Atmos. Chem. Phys., 14, 11949–11958, doi:10.5194/acp-14-11949-2014, 2014.

González Abad, G., Liu, X., Chance, K., Wang, H., Kurosu, T. P., and Suleiman, R.: Updated Smithsonian Astrophysical Observatory Ozone Monitoring Instrument (SAO OMI) formaldehyde retrieval, Atmos. Meas. Tech., 8, 19–32, doi:10.5194/amt-8-19-2015, 2015.

Gonzi, S., Palmer, P. I., Barkley, M. P., De Smedt, I., and Van Roozendael, M.: Biomass burning emission estimates inferred from satellite column measurements of HCHO: Sensitivity to co-emitted aerosol and injection height, Geophys. Res. Lett., 38, L14807, doi:10.1029/2011GL047890, 2011.

Hains, J. C., Boersma, K. F., Kroon, M., Dirksen, R. J., Cohen, R. C., Perring, A. E., Bucsela, E., Volten, H., Swart, D. P. J., Richter, A., Wittrock, F., Shoenhardt, A., Wagner, T., Ibrahim, O. W., Van Roozendael, M., Pinardi, G., Gleason, J. F., Veefkind, J. P., and Levelt, P.: Testing and improving OMI DOMINO tropospheric NO$_2$ using observations from the DANDELIONS and INTEX-B validation campaigns, J. Geophys. Res., 115, D05301, doi:10.1029/2009JD012399, 2010.

Han, K. M., Lee, S., Chang, L. S., and Song, C. H.: A comparison study between CMAQ-simulated and OMI-retrieved NO$_2$ columns over East Asia for evaluation of NO$_x$ emission fluxes of INTEX-B, CAPSS, and REAS inventories, Atmos. Chem. Phys., 15, 1913–1938, doi:10.5194/acp-15-1913-2015, 2015.

Hartl, A. and Wenig, M. O.: Regularisation model study for the least-squares retrieval of aerosol extinction time series from UV/VIS MAX-DOAS observations for a ground layer profile parameterisation, Atmos. Meas. Tech., 6, 1959–1980, doi:10.5194/amt-6-1959-2013, 2013.

Hassinen, S., Balis, D., Bauer, H., Begoin, M., Delcloo, A., Eleftheratos, K., Gimeno Garcia, S., Granville, J., Grossi, M., Hao, N., Hedelt, P., Hendrick, F., Hess, M., Heue, K.-P., Hovila, J., Jønch-Sørensen, H., Kalakoski, N., Kauppi, A., Kiemle, S., Kins, L., Koukouli, M. E., Kujanpää, J., Lambert, J.-C., Lang, R., Lerot, C., Loyola, D., Pedergnana, M., Pinardi, G., Romahn, F., van

Roozendael, M., Lutz, R., De Smedt, I., Stammes, P., Steinbrecht, W., Tamminen, J., Theys, N., Tilstra, L. G., Tuinder, O. N. E., Valks, P., Zerefos, C., Zimmer, W., and Zyrichidou, I.: Overview of the O3M SAF GOME-2 operational atmospheric composition and UV radiation data products and data availability, Atmos. Meas. Tech., 9, 383–407, doi:10.5194/amt-9-383-2016, 2016.

Heckel, A., Kim, S.-W., Frost, G. J., Richter, A., Trainer, M., and Burrows, J. P.: Influence of low spatial resolution a priori data on tropospheric NO_2 satellite retrievals, Atmos. Meas. Tech., 4, 1805–1820, doi:10.5194/amt-4-1805-2011, 2011.

Hendrick, F., Müller, J.-F., Clémer, K., Wang, P., De Mazière, M., Fayt, C., Gielen, C., Hermans, C., Ma, J. Z., Pinardi, G., Stavrakou, T., Vlemmix, T., and Van Roozendael, M.: Four years of ground-based MAX-DOAS observations of HONO and NO2 in the Beijing area, Atmos. Chem. Phys., 14, 765–781, doi:10.5194/acp-14-765-2014, 2014.

Herron-Thorpe, F. L., Lamb, B. K., Mount, G. H., and Vaughan, J. K.: Evaluation of a regional air quality forecast model for tropospheric NO_2 columns using the OMI/Aura satellite tropospheric NO_2 product, Atmos. Chem. Phys., 10, 8839–8854, doi:10.5194/acp-10-8839-2010, 2010.

Hewson, W., Bösch, H., Barkley, M. P., and De Smedt, I.: Characterisation of GOME-2 formaldehyde retrieval sensitivity, Atmos. Meas. Tech., 6, 371–386, doi:10.5194/amt-6-371-2013, 2013.

Holben, B. N., Eck, T. F., Slutsker, I., Tanre, D., Buis, J. P., Setzer, A., Vermote, E., Reagan, J. A., Kaufman, Y., Nakajima, T., Lavenu, F., Jankowiak, I., and Smirnov, A.: AERONET – A federated instrument network and data archive for aerosol characterization, Remote Sens. Environ., 66, 1–16, 1998.

Holben, B. N., Tanre, D., Smirnov, A., Eck, T. F., Slutsker, I., Abuhassan, N., Newcomb, W. W., Schafer, J., Chatenet, B., Lavenue, F., Kaufman, Y. J., Van de Castle, J., Setzer, A., Markham, B., Clark, D., Frouin, R., Halthore, R., Karnieli, A., O'Neill, N. T., Pietras, C., Pinker, R. T., Voss, K., and Zibordi, Z.: An emerging ground-based aerosol climatology: Aerosol optical depth from AERONET, J. Geophys. Res., 106, 12067–12097, 2001.

Hönninger, G. and Platt, U.: Observations of BrO and its vertical distribution during surface ozone depletion at Alert, Atmos. Environ., 36, 2481–2489, 2002.

Hönninger, G., von Friedeburg, C., and Platt, U.: Multi axis differential optical absorption spectroscopy (MAX-DOAS), Atmos. Chem. Phys., 4, 231–254, doi:10.5194/acp-4-231-2004, 2004.

Huang, R.-J., Zhang, Y., Bozzetti, C., Ho, K.-F., Cao, J., Han, Y., Dällenbach, K. R., Slowik, J. G., Platt, S. M., Canonaco, F., Zotter, P., Wolf, R., Pieber, S. M., Bruns, E. A., Crippa, M., Ciarelli, G., Piazzalunga, A., Schwikowski, M., Abbaszade, G., Schnelle-Kreis, J., Zimmermann, R., An, Z., Szidat, S., Baltensperger, U., Haddad, I. E., and Prévôt, A. S. H.: High secondary aerosol contribution to particulate pollution during haze events in China, Nature, 514, 218–222, 2014.

Irie, H., Kanaya, Y., Akimoto, H., Iwabuchi, H., Shimizu, A., and Aoki, K.: First retrieval of tropospheric aerosol profiles using MAX-DOAS and comparison with lidar and sky radiometer measurements, Atmos. Chem. Phys., 8, 341–350, doi:10.5194/acp-8-341-2008, 2008.

Irie, H., Takashima, H., Kanaya, Y., Boersma, K. F., Gast, L., Wittrock, F., Brunner, D., Zhou, Y., and Van Roozendael, M.: Eight-component retrievals from ground-based MAX-DOAS observa-

tions, Atmos. Meas. Tech., 4, 1027–1044, doi:10.5194/amt-4-1027-2011, 2011.

Irie, H., Boersma, K. F., Kanaya, Y., Takashima, H., Pan, X., and Wang, Z. F.: Quantitative bias estimates for tropospheric NO_2 columns retrieved from SCIAMACHY, OMI, and GOME-2 using a common standard for East Asia, Atmos. Meas. Tech., 5, 2403–2411, doi:10.5194/amt-5-2403-2012, 2012.

Irie, H., Muto, T., Itahashi, S., Kurokawa, J. I., and Uno, I.: Turnaround of Tropospheric Nitrogen Dioxide Pollution Trends in China, Japan, and South Korea, SOLA, 12, 170–174, doi:10.2151/sola.2016-035, 2016.

Jiang, C., Wang, H., Zhao, T., Li, T., and Che, H.: Modeling study of $PM_{2.5}$ pollutant transport across cities in China's Jing-Jin-Ji region during a severe haze episode in December 2013, Atmos. Chem. Phys., 15, 5803–5814, doi:10.5194/acp-15-5803-2015, 2015.

Jin, J., Ma, J., Lin, W., Zhao, H., Shaiganfar, R., Beirle, S., and Wagner, T.: MAX-DOAS measurements and satellite validation of tropospheric NO_2 and SO_2 vertical column densities at a rural site of North China, Atmos. Environ., 133, 12–25, 2016.

Junkermann, W.: On the distribution of formaldehyde in the western Po-Valley, Italy, during FORMAT 2002/2003, Atmos. Chem. Phys., 9, 9187–9196, doi:10.5194/acp-9-9187-2009, 2009.

Kanaya, Y., Irie, H., Takashima, H., Iwabuchi, H., Akimoto, H., Sudo, K., Gu, M., Chong, J., Kim, Y. J., Lee, H., Li, A., Si, F., Xu, J., Xie, P.-H., Liu, W.-Q., Dzhola, A., Postylyakov, O., Ivanov, V., Grechko, E., Terpugova, S., and Panchenko, M.: Long-term MAX-DOAS network observations of NO_2 in Russia and Asia (MADRAS) during the period 2007–2012: instrumentation, elucidation of climatology, and comparisons with OMI satellite observations and global model simulations, Atmos. Chem. Phys., 14, 7909–7927, doi:10.5194/acp-14-7909-2014, 2014.

Kaufman, Y. J., Tanré, D., and Boucher, O.: A satellite view of aerosols in the climate system, Nature, 419, 215–223, 2002.

Khokhar, M. F., Frankenberg, C., Van Roozendael, M., Beirle, S., Kühl, S., Richter, A., Platt, U., and Wagner, T., Satellite observations of atmospheric SO_2 from volcanic eruptions during the time-period of 1996–2002, Adv. Space Res., 36, 879–887, 2005.

Kleipool, Q. L., Dobber, M. R., de Haan, J., and Levelt, P. F.: Earth surface reflectance climatology from 3 years of OMI data, J. Geophys. Res.-Atmos., 113, D18308, doi:10.1029/2008JD010290, 2008.

Koukouli, M. E., Balis, D. S., Theys, N., Hedelt, P., Richter, A., Krotkov, N., Li, C., and Taylor, M.: Anthropogenic sulphur dioxide load over China as observed from different satellite sensors, Atmos. Environ., 145, 45–59, 2016.

Krotkov, N. A., Carn, S. A., Krueger, A. J., Bhartia, P. K., and Yang, K.: Band residual difference algorithm for retrieval of SO_2 from the Aura Ozone Monitoring Instrument (OMI), IEEE Geosci. Remote S., 44, 1259–1266, 2006.

Krotkov, N. A., McClure, B., Dickerson, R. R., Carn, S. A., Li, C., Bhartia, P. K., Yang, K., Krueger, A. J., Li, Z., Levelt, P. F., and Chen, H.: Validation of SO_2 retrievals from the Ozone Monitoring Instrument over NE China, J. Geophys. Res.-Atmos., 113, D16S40, doi:10.1029/2007JD008818, 2008.

Krueger, A. J., Walter, L. S., Bhartia, P. K., Schnetzler, C. C., Krotkov, N. A., Sprod, I. T., and Bluth, G. J. S.: Volcanic sulfur dioxide measurements from the total ozone mapping spectrom-

eter instruments, J. Geophys. Res.-Atmos., 100, 14057–14076, 1995.

Kurosu, T. P.: OMHCHO README FILE, available at: https://www.cfa.harvard.edu/atmosphere/Instruments/OMI/ PGEReleases/READMEs/OMHCHO_README.pdf (last access: 22 April 2016), 2008.

Lee, C., Martin, R. V., van Donkelaar, A., O'Byrne, G., Krotkov, N., Richter, A., Huey, L. G., and Holloway, J. S.: Retrieval of vertical columns of sulfur dioxide from SCIAMACHY and OMI: Air mass factor algorithm development, validation, and error analysis, J. Geophys. Res.-Atmos., 114, D22303, doi:10.1029/2009JD012123, 2009.

Leitão, J., Richter, A., Vrekoussis, M., Kokhanovsky, A., Zhang, Q. J., Beekmann, M., and Burrows, J. P.: On the improvement of NO$_2$ satellite retrievals – aerosol impact on the airmass factors, Atmos. Meas. Tech., 3, 475–493, doi:10.5194/amt-3-475-2010, 2010.

Levelt, P. F., Hilsenrath, E., Leppelmeier, G. W., van den Oord, G. H. J., Bhartia, P. K., Taminnen, J., de Haan, J. F., and Veefkind, J. P.: Science objectives of the Ozone Monitoring Instrument, IEEE Geosci. Remote S., 44, 1199–1208, 2006a.

Levelt, P. F., van den Oord, G. H. J., Dobber, M. R., Malkki, A., Visser, H., de Vries, J., Stammes, P., Lundell, J., and Saari, H.: The Ozone Monitoring Instrument, IEEE Geosci. Remote S., 44, 1093–1101, 2006b.

Li, C., Joiner, J., Krotkov, N. A., and Bhartia, P. K.: A fast and sensitive new satellite SO$_2$ retrieval algorithm based on principal component analysis: Application to the ozone monitoring instrument, Geophys. Res. Lett., 40, 6314–6318, 2013.

Li, X., Brauers, T., Hofzumahaus, A., Lu, K., Li, Y. P., Shao, M., Wagner, T., and Wahner, A.: MAX-DOAS measurements of NO$_2$, HCHO and CHOCHO at a rural site in Southern China, Atmos. Chem. Phys., 13, 2133–2151, doi:10.5194/acp-13-2133-2013, 2013.

Li, X., Brauers, T., Shao, M., Garland, R. M., Wagner, T., Deutschmann, T., and Wahner, A.: MAX-DOAS measurements in southern China: retrieval of aerosol extinctions and validation using ground-based in-situ data, Atmos. Chem. Phys., 10, 2079–2089, doi:10.5194/acp-10-2079-2010, 2010.

Lin, J.-T., McElroy, M. B., and Boersma, K. F.: Constraint of anthropogenic NO$_x$ emissions in China from different sectors: a new methodology using multiple satellite retrievals, Atmos. Chem. Phys., 10, 63–78, doi:10.5194/acp-10-63-2010, 2010.

Lin, J.-T., Martin, R. V., Boersma, K. F., Sneep, M., Stammes, P., Spurr, R., Wang, P., Van Roozendael, M., Clémer, K., and Irie, H.: Retrieving tropospheric nitrogen dioxide from the Ozone Monitoring Instrument: effects of aerosols, surface reflectance anisotropy, and vertical profile of nitrogen dioxide, Atmos. Chem. Phys., 14, 1441–1461, doi:10.5194/acp-14-1441-2014, 2014.

Lin, J.-T., Liu, M.-Y., Xin, J.-Y., Boersma, K. F., Spurr, R., Martin, R., and Zhang, Q.: Influence of aerosols and surface reflectance on satellite NO$_2$ retrieval: seasonal and spatial characteristics and implications for NO$_x$ emission constraints, Atmos. Chem. Phys., 15, 11217–11241, doi:10.5194/acp-15-11217-2015, 2015.

Lohmann, U. and Feichter, J.: Global indirect aerosol effects: a review, Atmos. Chem. Phys., 5, 715–737, doi:10.5194/acp-5-715-2005, 2005.

Loyola, D., Thomas, W., Livschitz, Y., Ruppert, T., Albert, P., and Hollmann, R.: Cloud properties derived from GOME/ERS-2 backscatter data for trace gas retrieval, IEEE Geosci. Remote S., 45, 2747–2758, doi:10.1109/TGRS.2007.901043, 2007.

Ma, J. Z., Beirle, S., Jin, J. L., Shaiganfar, R., Yan, P., and Wagner, T.: Tropospheric NO$_2$ vertical column densities over Beijing: results of the first three years of ground-based MAX-DOAS measurements (2008–2011) and satellite validation, Atmos. Chem. Phys., 13, 1547–1567, doi:10.5194/acp-13-1547-2013, 2013.

Martin, R. V., Jacob, D. J., Chance, K., Kurosu, T. P., Palmer, P. I., and Evans, M. J.: Global inventory of nitrogen oxide emissions constrained by space-based observations of NO$_2$ columns, J. Geophys. Res., 108, 4537, doi:10.1029/2003jd003453, 2003.

McCormic, R. A. and Ludwig, J. H.: Climate modifications by atmospheric aerosols, Science, 156, 1358–1359, 1967.

Millet, D. B., Jacob, D. J., Boersma, K. F., Fu, T.-M., Kurosu, T. P., Chance, K. V., Heald, C. L., and Guenther, A.: Spatial distribution of isoprene emissions from North America derived from formaldehyde column measurements by the OMI satellite sensor, J. Geophys. Res., 113, 1–18, doi:10.1029/2007JD008950, 2008.

Müller, J. F. and Brasseur, G.: IMAGES: A three-dimensional chemical transport model of the global troposphere, J. Geophys. Res.-Atmos., 100, 16445–16490, 1995.

Munro, R., Eisinger, M., Anderson, C., Callies, J., Corpaccioli, E., Lang, R., Lefebvre, A., Livschitz, Y., and Perez Albinana, A.: GOME-2 on MetOp: From in-orbit verification to routine operations, in: Proceedings of EUMETSAT Meteorological Satellite Conference, Helsinki, Finland, 1216, p. 48, 12–16 June 2006.

Munro, R., Lang, R., Klaes, D., Poli, G., Retscher, C., Lindstrot, R., Huckle, R., Lacan, A., Grzegorski, M., Holdak, A., Kokhanovsky, A., Livschitz, J., and Eisinger, M.: The GOME-2 instrument on the Metop series of satellites: instrument design, calibration, and level 1 data processing – an overview, Atmos. Meas. Tech., 9, 1279–1301, doi:10.5194/amt-9-1279-2016, 2016.

Nowlan, C. R., Liu, X., Chance, K., Cai, Z., Kurosu, T. P., Lee, C., and Martin, R. V.: Retrievals of sulfur dioxide from the Global Ozone Monitoring Experiment 2 (GOME-2) using an optimal estimation approach: Algorithm and initial validation, J. Geophys. Res.-Atmos., 116, D18301, doi:10.1029/2011JD015808, 2011.

Palmer, P. I., Jacob, D. J., Chance, K. V., Martin, R. V. D. R. J., Kurosu, T. P., Bey, I., Yantosca, R. M., and Fiore, A. M.: Air mass factor formulation for spectroscopic measurements from satellites: Application to formaldehyde retrievals from the Global Ozone Monitoring Experiment, J. Geophys. Res., 106, 14539–14550, doi:10.1029/2000JD900772, 2001.

Pinardi, G., Yu, H., Hendrick, F., Tack, F., Granville, J., Lambert, J.-C., and Van Roozendael, M.: End-to-end Validation of Total and Tropospheric NO$_2$ Columns from Atmospheric Composition Satellite Sensors, Atmospheric Composition Validation and Evolution, ESRIN, Italy, March 2013.

Platt, U. and Stutz, J.: Differential Optical Absorption Spectroscopy, Springer-Verlag, Heidelberg, Berlin, 229–375, 2008.

Richter, A., Burrows, J. P., Nüß, H., Granier, C., and Niemeier, U.: Increase in tropospheric nitrogen dioxide over China observed from space, Nature, 437, 129–132, 2005.

Richter, A., Wittrock, F., and Burrows, J. P.: SO$_2$ measurements with SCIAMACHY, in: Atmospheric Science Conference, Proceedings of the conference held 8–12 May 2006 at ESRIN, Fras-

cati Italy, edited by: Lacoste, H. and Ouwehand, L., ESA SP-628, European Space Agency, 2006.

Richter, A., Wittrock, F., Schönhardt, A., and Burrows, J. P.: Quantifying volcanic SO_2 emissions using GOME2 measurements, Geophys. Res. Abstr., EGU2009-7679, EGU General Assembly, 2009.

Rix, M., Valks, P., Hao, N., Loyola, D. G., Schlager, H., Huntrieser, H. H., Flemming, J., Koehler, U., Schumann, U., and Inness, A.: Volcanic SO_2, BrO and plume height estimations using GOME-2 satellite measurements during the eruption of Eyjafjallajökull in May 2010, J. Geophys. Res., 117, D00U19, doi:10.1029/2011JD016718, 2012.

Seinfeld, J. H. and Pandis, S. N.: Atmospheric Chemistry and Physics – From Air Pollution to Climate Change, John Wiley, New York, 1998.

Shaiganfar, R., Beirle, S., Sharma, M., Chauhan, A., Singh, R. P., and Wagner, T.: Estimation of NO_x emissions from Delhi using Car MAX-DOAS observations and comparison with OMI satellite data, Atmos. Chem. Phys., 11, 10871–10887, doi:10.5194/acp-11-10871-2011, 2011.

Spurr, R. J. D., Kurosu, T. P., and Chance, K. V.: A linearized discrete ordinate radiative transfer model for atmospheric remote-sensing retrieval, J. Quant. Spectrosc. Ra., 68, 689–735, 2001.

Spurr, R.: LIDORT and VLIDORT: Linearized pseudo-spherical scalar and vector discrete ordiate radiative transfer models for use in remote sensing retrieval problems, in: Light Scattering Reviews 3 , edited by: Kokhanovsky, A., 229–275, Springer, Berlin, doi:10.1007/978-3-540-48546-9_7, 2008.

Stammes, P.: Errors in UV reflectivity and albedo calculations due to neglecting polarisation, SPIE, 2311, 227–235, doi:10.1117/12.198580, 1994.

Stammes, P., Sneep, M., de Haan, J. F., Veefkind, J. P., Wang, P., and Levelt, P. F.: Effective cloud fractions from the Ozone Monitoring Instrument: Theoretical framework and validation, J. Geophys. Res., 113, D16S38, doi:10.1029/2007JD008820, 2008.

Stavrakou, T., Müller, J.-F., Boersma, K. F., van der A, R. J., Kurokawa, J., Ohara, T., and Zhang, Q.: Key chemical NO_x sink uncertainties and how they influence top-down emissions of nitrogen oxides, Atmos. Chem. Phys., 13, 9057–9082, doi:10.5194/acp-13-9057-2013, 2013.

Stavrakou, T., Müller, J.-F., Bauwens, M., De Smedt, I., Van Roozendael, M., De Mazière, M., Vigouroux, C., Hendrick, F., George, M., Clerbaux, C., Coheur, P.-F., and Guenther, A.: How consistent are top-down hydrocarbon emissions based on formaldehyde observations from GOME-2 and OMI?, Atmos. Chem. Phys., 15, 11861–11884, doi:10.5194/acp-15-11861-2015, 2015.

Theys, N., De Smedt, I., Gent, J., Danckaert, T., Wang, T., Hendrick, F., Stavrakou, T., Bauduin, S., Clarisse, L., Li, C., Krotkov, N., Yu, H., Brenot, H., and Van Roozendael, M.: Sulfur dioxide vertical column DOAS retrievals from the Ozone Monitoring Instrument: Global observations and comparison to ground-based and satellite data, J. Geophys. Res.-Atmos., 120, 2470–2491, 2015.

Valks, P., Pinardi, G., Richter, A., Lambert, J.-C., Hao, N., Loyola, D., Van Roozendael, M., and Emmadi, S.: Operational total and tropospheric NO2 column retrieval for GOME-2, Atmos. Meas. Tech., 4, 1491–1514, doi:10.5194/amt-4-1491-2011, 2011.

van der A, R. J., Eskes, H. J., Boersma, K. F., Van Noije, T. P. C., Van Roozendael, M., De Smedt, I., Peters, D. H. M.

U., and Meijer, E. W.: Trends, seasonal variability and dominant NOx source derived from a ten year record of NO_2 measured from space, J. Geophys. Res.-Atmos., 113, D04302, doi:10.1029/2007JD009021, 2008.

Van Roozendael, M., Fayt, C., Post, P., Hermans, C., and Lambert, J.-C.: Retrieval of BrO and NO_2 from UV-Visible Observations, in: Sounding the troposphere from space: a new Era for Atmospheric Chemistry. The TROPOSAT Final Report, edited by: Borrell, P., Borrell, P. M., Burrows, J. P., and Platt, U., Springer Verlag, Berlin, Heidelberg, 155–166, 2003.

Veefkind, J. P., Aben, I., McMullan, K., Förster, H., De Vries, J., Otter, G., Claas, J., Eskes, H. J., De Haan, J. F., Kleipool, Q., and Van Weele, M.: TROPOMI on the ESA Sentinel-5 Precursor: A GMES mission for global observations of the atmospheric composition for climate, air quality and ozone layer applications, Remote Sens. Environ., 120, 70–83, 2012.

Vlemmix, T., Piters, A. J. M., Stammes, P., Wang, P., and Levelt, P. F.: Retrieval of tropospheric NO_2 using the MAX-DOAS method combined with relative intensity measurements for aerosol correction, Atmos. Meas. Tech., 3, 1287–1305, doi:10.5194/amt-3-1287-2010, 2010.

Vlemmix, T., Piters, A. J. M., Berkhout, A. J. C., Gast, L. F. L., Wang, P., and Levelt, P. F.: Ability of the MAX-DOAS method to derive profile information for NO_2: can the boundary layer and free troposphere be separated?, Atmos. Meas. Tech., 4, 2659–2684, doi:10.5194/amt-4-2659-2011, 2011.

Vlemmix, T., Eskes, H. J., Piters, A. J. M., Schaap, M., Sauter, F. J., Kelder, H., and Levelt, P. F.: MAX-DOAS tropospheric nitrogen dioxide column measurements compared with the Lotos-Euros air quality model, Atmos. Chem. Phys., 15, 1313–1330, doi:10.5194/acp-15-1313-2015, 2015a.

Vlemmix, T., Hendrick, F., Pinardi, G., De Smedt, I., Fayt, C., Hermans, C., Piters, A., Wang, P., Levelt, P., and Van Roozendael, M.: MAX-DOAS observations of aerosols, formaldehyde and nitrogen dioxide in the Beijing area: comparison of two profile retrieval approaches, Atmos. Meas. Tech., 8, 941–963, doi:10.5194/amt-8-941-2015, 2015b.

Wagner, T., Dix, B., von Friedeburg, C., Frieß, U., Sanghavi, S., Sinreich, R., and Platt, U.: MAX-DOAS O_4 measurements: A new technique to derive information on atmospheric aerosols – Principles and information content, J. Geophys. Res., 109, D22205, doi:10.1029/2004JD004904, 2004.

Wagner, T., Beirle, S., Brauers, T., Deutschmann, T., Frieß, U., Hak, C., Halla, J. D., Heue, K. P., Junkermann, W., Li, X., Platt, U., and Pundt-Gruber, I.: Inversion of tropospheric profiles of aerosol extinction and HCHO and NO_2 mixing ratios from MAX-DOAS observations in Milano during the summer of 2003 and comparison with independent data sets, Atmos. Meas. Tech., 4, 2685–2715, doi:10.5194/amt-4-2685-2011, 2011.

Wagner, T., Apituley, A., Beirle, S., Dörner, S., Friess, U., Remmers, J., and Shaiganfar, R.: Cloud detection and classification based on MAX-DOAS observations, Atmos. Meas. Tech., 7, 1289–1320, doi:10.5194/amt-7-1289-2014, 2014.

Wang, P., Stammes, P., van der A, R., Pinardi, G., and van Roozendael, M.: FRESCO+: an improved O2 A-band cloud retrieval algorithm for tropospheric trace gas retrievals, Atmos. Chem. Phys., 8, 6565–6576, doi:10.5194/acp-8-6565-2008, 2008.

Wang, Y., Li, A., Xie, P. H., Chen, H., Xu, J., Wu, F. C., Liu, J. G., and Liu, W. Q.: Retrieving vertical profile of aerosol extinction

by multi-axis differential optical absorption spectroscopy, Acta Phys. Sin., 16, doi:10.7498/aps.62.180705, http://wulixb.iphy.ac.cn/EN/abstract/abstract54703.shtml#, 2013a.

Wang, Y., Li, A., Xie, P. H., Chen, H., Mou, F. S., Xu, J., Wu, F. C., Zeng, Y., Liu, J. G., and Liu, W. Q.: Measuring tropospheric vertical distribution and vertical column density of NO$_2$ by multi-axis differential optical absorption spectroscopy, Acta Phys. Sin., 16, doi:10.7498/aps.62.200705, http://wulixb.iphy.ac.cn/EN/abstract/abstract56201.shtml, 2013b.

Wang, Y., Li, A., Xie, P. H., Wagner, T., Chen, H., Liu, W. Q., and Liu, J. G.: A rapid method to derive horizontal distributions of trace gases and aerosols near the surface using multi-axis differential optical absorption spectroscopy, Atmos. Meas. Tech., 7, 1663–1680, doi:10.5194/amt-7-1663-2014, 2014.

Wang, Y., Penning de Vries, M., Xie, P. H., Beirle, S., Dörner, S., Remmers, J., Li, A., and Wagner, T.: Cloud and aerosol classification for 2.5 years of MAX-DOAS observations in Wuxi (China) and comparison to independent data sets, Atmos. Meas. Tech., 8, 5133–5156, doi:10.5194/amt-8-5133-2015, 2015.

Wang, Y., Lampel, J., Xie, P., Beirle, S., Li, A., Wu, D., and Wagner, T.: Ground-based MAX-DOAS observations of tropospheric aerosols, NO$_2$, SO$_2$ and HCHO in Wuxi, China, from 2011 to 2014, Atmos. Chem. Phys., 17, 2189–2215, doi:10.5194/acp-17-2189-2017, 2017.

Williams, J. E., Scheele, M. P., van Velthoven, P. F. J., Cammas, J.-P., Thouret, V., Galy-Lacaux, C., and Volz-Thomas, A.: The influence of biogenic emissions from Africa on tropical tropospheric ozone during 2006: a global modeling study, Atmos. Chem. Phys., 9, 5729–5749, doi:10.5194/acp-9-5729-2009, 2009.

Wittrock, F., Oetjen, H., Richter, A., Fietkau, S., Medeke, T., Rozanov, A., and Burrows, J. P.: MAX-DOAS measurements of atmospheric trace gases in Ny-Ålesund – Radiative transfer studies and their application, Atmos. Chem. Phys., 4, 955–966, doi:10.5194/acp-4-955-2004, 2004.

Wittrock, F., Richter, A., Oetjen, H., Burrows, J. P., Kanakidou, M., Myriokefalitakis, S., Volkamer, R., Beirle, S., Platt, U., and Wagner, T.: Simultaneous global observations of glyoxal and formaldehyde from space, Geophys. Res. Lett., 33, L16804, doi:10.1029/2006GL026310, 2006a.

Wittrock, F.: The Retrieval of Oxygenated Volatile Organic Compounds by Remote Sensing Techniques, PhD, University of Bremen, Bremen, Germany, available at: http://www.doas-bremen.de/paper/diss_wittrock_06.pdf (last access: 9 April 2017), 2006b.

Xue, L., Ding, A., Gao, J., Wang, T., Wang, W., Wang, X., Lei, H., Jin, D., and Qi, Y.: Aircraft measurements of the vertical distribution of sulfur dioxide and aerosol scattering coefficient in China, Atmos. Environ., 44, 278–282, 2010.

Yang, K., Krotkov, N. A., Krueger, A. J., Carn, S. A., Bhartia, P. K., and Levelt, P. F.: Retrieval of large volcanic SO$_2$ columns from the Aura Ozone Monitoring Instrument: Comparison and limitations, J. Geophys. Res.-Atmos., 112, D24S43, doi:10.1029/2007JD008825, 2007.

Yilmaz, S.: Retrieval of Atmospheric Aerosol and Trace Gas Vertical Profiles using Multi-Axis Differential Optical Absorption Spectroscopy, Dissertation submitted to the Combined Faculties for the Natural Sciences and for Mathematics of the Ruperto-Carola University of Heidelberg, Germany for the degree of Doctor of Natural Sciences, 2012.